Student thesis series INES nr 527

A remote-sensing approach to studying drought resistance in Swedish old-growth and production forests

Julika Wolf

2020
Department of
Physical Geography and Ecosystem Science
Lund University
Sölvegatan 12
S-223 62 Lund
Sweden

Julika Wolf (2020).

A remote-sensing approach to studying drought resistance in Swedish old-growth and production forests

Master degree thesis, 30 credits in *Physical Geography and Ecosystem Science*
Department of Physical Geography and Ecosystem Science, Lund University

Level: Master of Science (MSc)

Course duration: *23 March* 2020 until *5 August* 2020

Disclaimer

A remote-sensing approach to studying drought resistance in Swedish old-growth and production forests

---

Julika Wolf

Master thesis, 30 credits, in *Physical Geography and Ecosystem Analysis*

Supervisors

Anders Ahlström
Dep. of Physical Geography and Ecosystem Science, Lund University

Feng Tian
Dep. of Physical Geography and Ecosystem Science, Lund University

Exam committee

Lina Eklund, Dep. of Physical Geography and Ecosystem Science, LU
Sofia Junttila, Dep. of Physical Geography and Ecosystem Science, LU

Acknowledgements

"It is by logic that we prove, but by intuition that we discover"

Inspirational quote seen carved into a park bench.
Burney Falls State Park, around Pacific Crest Trail km 2,200

A little over two years ago, I decided to go on a very long walk. More precisely, I walked from Mexico to Canada on the Pacific Crest Trail, which stretches over 4,280km across California, Oregon, and Washington. I think that the decision to hike was partly based on some sort of romantic idealism of getting to know my 'study subject' in a very different, maybe deeper and more intuitive, way, than a classroom setting would allow for. And I did succeed with that aspiration. I had never actually been out in the backcountry for an extended period before, and never had I experienced anything remotely resembling the last old-growth forests as you find them in the Pacific Northwest. I remember every-day life consisting of cursing and scrambling over more fallen trees left to decompose than a professional hurdle athlete, and this silly running-gag pun of searching for the oldest, and most peculiar looking individuals, only to yell "Gnarly Bro!" with my best Australian surfer accent (all of that while shoving copious amounts of huckleberries into my mouth). Over the course of five months, I discovered a sense of home as never experienced before, as it was felt for an ecosystem, rather than a specific place or town. All along, I was already admitted to the Master program in Lund, and I felt extremely excited about the prospect of re-encountering on an intellectual level what I was experiencing very viscerally. I vowed to myself to never forget that (or at least try), and the memory of that vow is probably what kept me sane throughout the more stressful moments of this thesis. I would therefore like to thank the PCTA and their incredible efforts of maintaining the PCT, as well as Jonathan Seaquist and Ulrik Mårtensson for helping me with my request for an official deferment, which enabled me to complete the trail and join the department after the semester had already begun (and consequently, to write this thesis with an individualized schedule). Moreover, I would like to thank Princess, Cowboy, Cheez-It, Monster, and Stroll for their companionship, shared love for the outdoors, and practical help in taking on the logistics of organizing my move to Sweden (such as night-hiking along exposed ridge-lines to find strong enough cell service for a hotspot so I could apply in time for student housing!).

Having said this, I nevertheless entered a (maybe healthy) phase of disillusion about academia. That realization was scary, especially as it came right around the time when I ought to pick a thesis topic. Therefore, a big thank you to my supervisor Anders Ahlström, not just for your excellent supervision throughout the project, but also for your eccentricity and lightheartedness, as well as your audacity to think 'big' and outside the box, which were probably the even more valuable and much needed lessons to be learned here to get back on track. Moreover, I would like to thank my co-supervisor Feng Tian for his helpful feedback regarding the remote sensing technicalities throughout the project, and Carl-Fredrik Johannesson for paving the way with his excellent thesis on biomass storage in Swedish old-growth forests, and the advice he passed on to me. Lastly, I would like to thank Steven Deléglise for never ceasing to come up with new ideas for fun (non-thesis) activities and for ensuring that I don't overwork myself.

Abstract

Boreal forest ecosystems are predicted to experience hotter and drier summers due to climate change, leading to more frequently reduced soil water availability and an increased risk of droughts, as was already the case in Northern Europe during the severe summer drought of 2018. Prolonged water stress in forest ecosystems can lead to impacts ranging from reduced photosynthesis to forest dieback. However, it is currently unknown whether characteristics associated with undisturbed old-growth forests, such as a natural age structure, and the presence of understory and dead wood, are linked to increased drought resistance. Therefore, this study investigated 2018 drought impacts of over 300 Swedish forest pairs through a comparative analysis of spatially proximate old-growth and production forest stands, and their associated Landsat EVI2 Z-scores. Prior to this, several candidate satellite vegetation indices (Landsat EVI2, MODIS EVI2, MODIS NDWI, MODIS CCI) were evaluated on their ability to capture anomalies in gross primary production (GPP) measured at different Eddy-Covariance ecosystem monitoring stations. The candidate indices were also compared at the landscape level across a highly heterogenous 'case study' area in northern Sweden. While neither of the indices consistently captured GPP anomalies at the tested stations, the increasingly degraded spatial resolution associated with the MODIS vegetation indices proved to cause severe smoothing effects when investigating impacts across a topographically varied landscape; in contrast, Landsat EVI2 captured negative anomalies along drier slopes, while moister valleys were associated with positive Z-scores. It was therefore chosen as the most suitable index, and for further analysis, forested areas were separated into five distinct topographical soil moisture classes. Despite their older age, old-growth forests were on average associated with significantly higher Z-scores than their surrounding production forests. Overall Z-scores increased with increasing soil moisture, whereas relative differences (old-growth – production Z-score per forest pair) decreased. When normalized by the frequency distribution of the soil moisture classes, the mean difference amounted to +0.13. Furthermore, variability in drought impacts was higher for old-growth than production forests, and consequently, both the stands associated with the highest positive and negative anomalies were old-growth. The largest negative Z-score differences can be reconciled by the fact that those old-growth forests were on significantly steeper slopes and had a higher fraction of purely deciduous stands. Apart from that, however, relative differences in drought impacts were not associated with a clear spatial pattern, and no general relationship was found with drought severity, nor relative differences in age, elevation, and slope. Differences were therefore likely caused by other factors not considered.

Key words

Physical Geography and Ecosystem Analysis, drought impacts, vegetation water stress, old-growth forests, forest management, resilience, resistance, climate change, boreal forests, remote sensing, GPP

Table of Contents

List of abbreviations

B	Blue reflectance (0.4-0.5µm)
CCI	Chlorophyll/Carotenoid Index
DEM	Digital Elevation Model
EVI	Enhanced Vegetation Index
EVI2	Two-band version of Enhanced Vegetation Index
fAPAR	Fraction of absorbed photosynthetically active radiation
GEE	Google Earth Engine
GPP	Gross Primary Production
LAI	Leaf Area Index
LHF	Latent heat flux
MODIS	Moderate Resolution Imaging Spectroradiometer
NDVI	Normalized Difference Vegetation Index
NDWI	Normalized Difference Water Index
NEE	Net Ecosystem Exchange
NIR	Near-infrared spectral region (0.7-1.2µm)
PRI	Photochemical Reflectance Index
R	Red reflectance (0.6-0.7µm)
RS	Remote Sensing
scPDSI	Self-calibrating Palmer Drought Severity Index
SM	Soil moisture
SPI	Standardized Precipitation Index
SWIR	Shortwave infrared spectral region (about 1.3-2.5µm)
TWI	Topographical Wetness Index
VI	Vegetation Index
VIS	Visible spectral region (0.4 - 0.7µm)

1. Introduction

Boreal forest ecosystems are predicted to experience hotter summers due to climate change, and while precipitation is predicted to increase to a moderate extent as well, this will be insufficient to compensate for the increased evapotranspiration caused by changes in temperature (Gauthier et al. 2015). Such warmer and drier conditions lead to more frequently reduced soil water availability and increase the risk of droughts (Seidl et al. 2017), as was already the case in large parts of Central and Northern Europe during the summer drought of 2018 (Reinermann et al. 2019).

One coping mechanism of plants during periods of water stress is to partially close their stomata, thus reducing evaporative water loss and photosynthetic carbon uptake (Peters et al. 2018). In fact, numerous Scandinavian ecosystem monitoring stations reported decreased Net Ecosystem Production during the summer of 2018, with some of the monitored forests changing from carbon sinks to sources (Linderson et al. 2020). However, the understanding of the response of forest carbon and water fluxes to a warmer and drier climate is still far from complete (Grossiord et al. 2013).

One key missing aspect is the role that functional diversity plays in forest resilience and resistance to drought; resilience hereby refers to the capacity of a forest to return to pre-drought growth conditions, while resistance refers to the ability to withstand a drought during its occurrence (Vanhellemont et al. 2019). While some studies suggest a buffering effect through higher hydraulic diversity and increased drought resistance through reduced competition in more heterogenous stands (Gazol et al. 2016; Anderegg et al. 2018), the opposite could be the case, with for instance mixed forests more quickly exhausting available soil water than monospecific stands (Grossiord et al. 2013). Studies conducted so far have focused on labor-intensive tree ring and carbon isotope analyses and their conclusions are therefore to a large extent based on relatively small sample sizes and limited areas; furthermore, the majority of research on drought resistance so far only compared stands within secondary forests that have been altered by human disturbance, therefore constituting systems that likely function very differently than old-growth forest stands. The latter are typically characterized by natural succession, by the increased presence of older trees, dead wood, and understory (Hedwall et al. 2010; Sabatini et al. 2018) and it is unknown to what extent these differences between old-growth forests and forests that are managed for production purposes through measures such as thinning and drainage, influence drought resistance.

Satellite remote sensing (RS) has increasingly been employed to study the effects of disturbances on ecosystems through utilization of so-called vegetation indices (VI), which are designed to capture spectral changes caused by changes in vegetation characteristics (AghaKouchak et al. 2015). Since water stress can lead to reduced leaf water content and altered pigment pools,

detectable in the shortwave-infrared (SWIR) and visible (VIS) spectral regions, previous RS studies successfully quantified past drought impacts in various European countries (e.g. Reichstein et al. 2007; Dotzler et al. 2015; Puletti et al. 2019; Reinermann et al. 2019). However, to our knowledge, no study so far has explicitly investigated differences in drought resistance between old-growth forests and production forests through the use of satellite RS data, despite the urgent need to fill this knowledge gap, given the likelihood of more frequent droughts in the near future, and the data abundance RS offers when compared to in-situ methods. Therefore, the aim of this thesis is twofold: firstly, a suitable vegetation index to study drought impacts in Scandinavian forests will be identified, the latter being typically characterized by highly fragmented landscapes and an abundance of evergreen coniferous tree species, which not necessarily show discoloration during drought stress. In combination, this makes the choice of a suitable VI and satellite sensor and its associated tradeoff between available spectral, temporal, and spatial resolution particularly challenging. In order to investigate this, temporal anomalies of various potential candidate VIs will be studied at different Scandinavian ecosystem monitoring stations, to test whether they successfully capture local anomalies of gross primary production (GPP). Furthermore, the candidate VIs will be evaluated at the landscape level across a highly heterogenous 'case study' area in northern Sweden. Subsequently, the most suitable VI identified in part one will be utilized to compare drought impacts in Sweden's last remaining old-growth and their surrounding production forests, based on a newly available map holding detailed information on the locations of Swedish old-growth forests. In short, the following two research questions will be addressed:

1. What is the most suitable vegetation index to study 2018 drought impacts on Swedish forests?
2. Are old-growth forests more drought resistant than their surrounding production forests?

2. Background

2.1. Swedish old-growth and production forests

Forests currently cover over 60% of Sweden's total area, making it by far the most abundant land-cover class. At the same time, the majority of Swedish forests are managed for commercial purposes; in fact, the Swedish forestry sector currently supplies about ten percent of the global sawn timber, pulp, and paper products, making these products one of the country's most important export revenues (KSLA 2015; Lindahl et al. 2017).

Forests have long played an important role in the countries' economic development; for centuries, areas were cleared for use as firewood, for farming, or directly used for forest grazing; with

industrialization, timber was increasingly needed as fuel for the mining, iron, and steel industry, for charcoal and tar production, in the shipping industry, and starting in the late 1800s, for the manufacturing of pulp and paper, among other uses (KSLA 2015). Consequently, by the early 20th century, most of Sweden's forests were left degraded, with parts of southern Sweden essentially devoid of any forest. To alleviate the situation, the national Forestry Act was established in 1903, primarily aimed at improving forest management to ensure a steady supply to meet industrial demands (Eriksson et al. 2018), and until the early 90s, silvicultural measures to be applied during different rotational stages were strongly regulated (Lindahl et al. 2017). While these efforts successfully led to almost a doubling in standing tree volume over the past century (Jonsson et al. 2011), its legacy today is a forest management regime largely dominated by single-species, even-aged forest stands of Scots pine (*Pinus sylvestris*) and Norway spruce (*Picea abies)*, which are replanted following a clear-cut, typically succeeded by several rounds of thinning and cleaning, and eventually clear-cut again after 60-120 years (Vestin 2017). Furthermore, selection of fast-growing, damage-resistant phenotypes and fertilization (KSLA 2015) are common practices, as well as the extensive drainage of wetter areas, artificially lowering water tables to promote tree growth and avoid water-logging after clear-cutting has occurred (Jacks 2019). Thus, most of Sweden's extensive forest landscape is structurally very different from what would be found naturally, with only few 'natural' forests left *'like islands within managed forests'* (Fridman 2000, p. 95) scattered throughout the country (Figure 1).

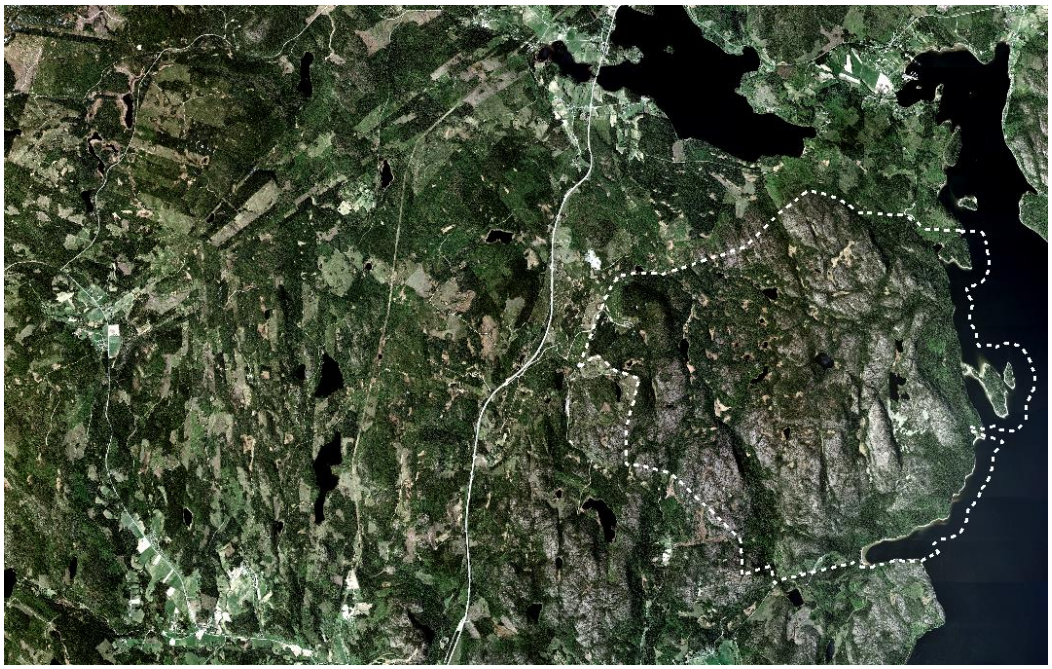

Figure 1: Orthophoto showing a forest landscape in Västernorrland County, near the coast of the Baltic Sea. Skuleskogen national park (park boundaries shown as dashed lines) is readily distinguished as a patch of old-growth forest amidst a complex patchwork of clear-cut areas and production forests at different rotational stages. Source orthophoto: © Lantmäteriet (2012).

Primary forests, here interchangeably referred to as ‘old-growth’ forests, are generally defined as naturally regenerated forests of native species without visible traces of past human disturbance, with key characteristics being the presence of dead wood, as well as a natural age structure (FAO 2015). This will be used as the operational definition for the remainder of this project; however, note that other definitions encompass additional criteria on, for instance, minimum area, and discrepancies between terminologies exist (Buchwald 2005). In a recent study, the boreal biome was found to host the majority of Europe’s last old-growth forests; despite Sweden’s extensive forest management history, Sweden is believed to still host the largest continuous stretches of old-growth forest in Europe (Sabatini et al. 2018), although to date, no official map showing the current extent of these forests, exists.

2.2. Northern forests in a warming world

2.2.1 A portrait of the 2018 drought and its impacts

While droughts are commonly connected to a deficiency in precipitation over a sustained time period, there is no single, overarching definition of the term; instead, the phenomenon can be understood through four operational definitions, depending on the variable used to describe its occurrence: 1) meteorological droughts, characterized by a sustained lack of precipitation, 2) hydrological droughts, that is, a diminished surface water flow, 3) agricultural droughts, where crop growth is affected through reduced soil moisture, and 4) socio-economic droughts, due to failure of meeting water demands (Mishra and Singh 2010). For the remainder of this project, the term should be understood as referring to the definitions of a meteorological/agricultural drought.

In contrast to the extreme heatwave in Europe in 2003, temperature and precipitation anomalies during the summer of 2018 displayed a bimodal distribution, with Central and Northern Europe experiencing extreme heat, while the Mediterranean and Iberian Peninsula experienced normal conditions and negative anomalies, respectively (Buras et al. 2020). The drought was onset by a dry-spell and above-average temperatures in May through the establishment of a persistent high-pressure system, with the situation worsening throughout June and July (Masante and Vogt 2018b). In August and September, parts of Northern Europe recovered somewhat, while the situation persisted in several Central European countries until October (Masante and Vogt 2018c). Furthermore, in Scandinavia, the drought had been preceded by a lack of precipitation from March onwards already, thus developing over a longer time period (Masante and Vogt 2018a). Sweden experienced positive temperature anomalies of up to 4°C, with July being the hottest month measured on record for several parts of the country. Precipitation anomalies showed a more heterogenous distribution, whereby the northwestern part of the country, as well as parts along the

Bothnian Coastline received above-average rainfall in June, with some areas in Lapland experiencing the rainiest summer in decades. In contrast, parts of southern Sweden received less than half of their normal precipitation. At the end of an otherwise dry August, heavy rainfalls over southern Sweden normalized monthly precipitation values within a short time period (SMHI 2018a). An overview of the progression of the 2018 monthly temperature and precipitation anomalies for the months May to August is shown in Figure 2.

As a consequence of the drought, central Sweden experienced several severe forest fires (SMHI 2018a), as well as devastating impacts on agricultural yields, and the situation was declared a national crisis (Regeringskansliet 2019). However, impacts on other ecosystems, including forests, remain to be explored. A first Europe-wide quantification of 2018 ecosystem impacts based on Moderate Resolution Imaging Spectroradiometer (MODIS) RS data estimated the total most severely affected area to be twice as large as compared to 2003, as well as the coupling between the climatic water balance and drought impacts to be stronger than in 2003 (Buras et al. 2020). Consequently, the authors hypothesized that the scale of impacts was likely a function of the location of the drought, where during the summer of 2003, the epicenter hit Mediterranean ecosystems that are better adapted to such conditions than is the case for northern forests. In fact, an earlier study on southern Scandinavian Norway spruce trees revealed severe hydraulic dysfunction, top dieback, and stem cracking emerging as a long-term consequence of a dry-spell during the summer of 2006 (Rosner et al. 2018). 2018 being unprecedented in recent Swedish meteorological history, similar or more severe impacts are to be expected. Importantly, drought-induced hydraulic dysfunction has been shown to be a mediator of subsequent delayed forest dieback, where mortality often only peaks several years after the drought event took place (Anderegg et al. 2019). Moreover, drought-induced vulnerability can act as a facilitator for other subsequent disturbances such as insect and pest outbreaks, indirectly amplifying drought impacts (Seidl et al. 2017). Thus, while the focus of this thesis is to study forest resistance in the context of the short-term effects of the 2018 drought, observed tree stress will likely be an underestimation of the real magnitude of impacts, with increased mortality events likely to be observable only in the years to come.

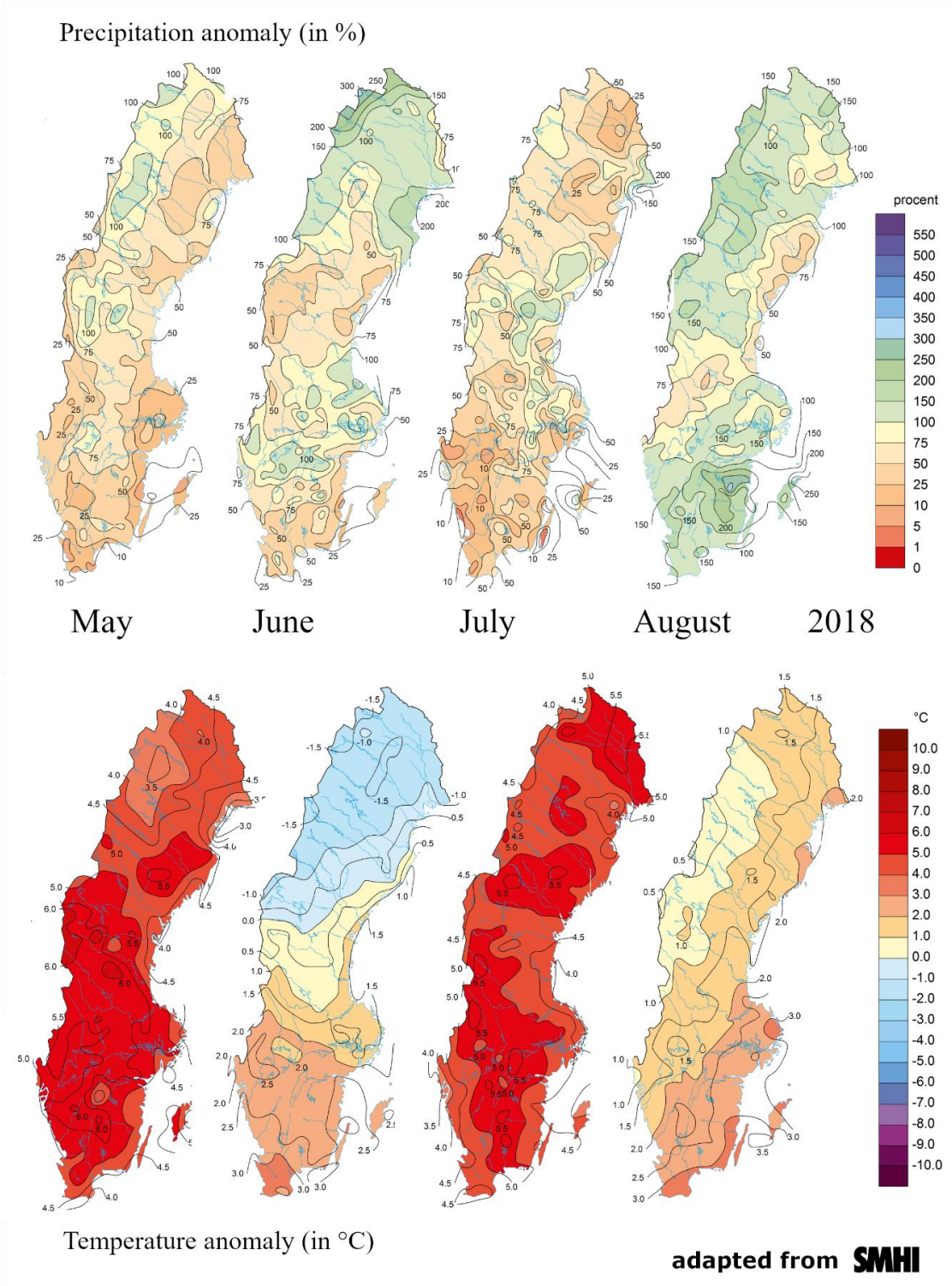

Figure 2. Spatial variability of monthly precipitation (upper panel) and temperature (lower panel) anomalies over Sweden during the 2018 drought, showing its progression from May – August. Monthly means during the 1961-1990 period are used as baseline. Note the exponential scale of the precipitation anomaly values. Adapted from the original maps of SMHI (2018b), permission received

2.2.2 Linking forest drought stress to the carbon cycle

Plant water stress can be induced by atmospheric vapor pressure deficit (VPD) on a scale of days to weeks, and further aggravated by soil moisture limitations on a seasonal time scale. Such conditions trigger stomatal closure, which increases the plant's intrinsic water use efficiency and aids to slow down further water loss through evapotranspiration (Peters et al. 2018). At the same time, carbon dioxide uptake is hampered, leading to reduced photosynthesis. If dry conditions continue to prevail, pressure in the water-transporting xylem tissue falls and cavitation, i.e. a phase-change from liquid water to vapor, occurs. Such xylem embolism impedes further water transport and photosynthesis, leading to tissue damage, desiccation, and in some cases, carbon starvation and eventual tree death (Choat et al. 2012; Trugman et al. 2018).

During the summer of 2018, ground water levels in Southern Sweden were critically low for extended time periods (Belyazid and Giuliana 2019), and several Scandinavian ecosystem monitoring stations measuring ecosystem-atmosphere carbon exchange by means of Eddy-Covariance flux towers recorded a strong weakening of the forests' ability to act as atmospheric carbon sinks (Linderson et al. 2020), thus indicating severe local drought stress reactions. This stands in stark contrast to what happened in 2003, where Swedish forests showed an increase in the rate of photosynthetic carbon uptake, commonly expressed as Gross Primary Production (GPP), where water was not as limited, while the rest of Europe experienced an estimated 30% decrease of GPP, reversing four years of carbon sequestration (Ciais et al. 2005). Albeit a still poorly constrained number, forests are estimated to currently act as a sink of 29% of annual anthropogenic carbon emissions due to CO_2 fertilization and a lengthening of the growing season (Friedlingstein et al. 2019). A long-held paradigm hereby regards old-growth forests as carbon neutral due to reduced growth rates and increased maintenance respiration of older trees, therefore excluding them from the carbon budget. However, recent research suggests that this view is unsupported, and that both temperate and boreal old-growth forests continue to accumulate carbon over centuries, thus storing vast carbon stocks (Luyssaert et al. 2008). Given that droughts are predicted to occur more frequently due to climate change and boreal forests are under substantial threat under a drier future climate (Gauthier et al. 2015; Seidl et al. 2017), whether old-growth forests are able to withstand prolonged dry spells and retain their ability to function as a net carbon sink, is thus of key importance for the global carbon budget.

2.3. Factors influencing forest drought resistance

Throughout the last two decades, an intensified research effort motivated by the accelerated loss of biodiversity has led to the recognition of biodiversity as one of the most important determinants of ecosystem functioning (Tilman et al. 2014). In principle, changes in species and functional group diversity can lead to a combination of both negative and positive effects on ecosystems (Loreau and Hector 2001; Grossiord et al. 2013). On the one hand, increased occurrence of so-called 'niche complementarity' in diverse ecosystems, that is, niche separation and facilitative species interactions, generally leads to decreased competition, more efficient partitioning of resources, and to increases in overall community performance (Loreau and Hector 2001). Moreover, the 'insurance hypothesis' predicts that if conditions change, at least some species are likely to persist, stabilizing overall community functioning (Tilman et al. 2014; Anderegg et al. 2018). For instance, tree growth in several European forest stands has been shown to be less variable through time in mixed stands, where species diversity stabilized overall wood production under a wider range of environmental conditions (Jucker et al. 2014). On the other hand, increased competition can lead to a 'selection effect' and to the dominance of a single species with a particular – beneficial or harmful – trait (Loreau and Hector 2001); furthermore, if niches of coexisting species are overlapping, direct competition can lead to quicker resource depletion (Grossiord et al. 2013).

Therefore, whether such contrasting interaction effects end up enhancing or reducing overall drought resilience and resistance of forests is currently a topic of active debate, fueled by inconsistent research findings. A recent paper by Anderegg et al. (2018) showed that temperate and boreal forests with a higher diversity in hydraulic traits exhibit a buffering effect on latent heat flux (LHF) variations during dry periods, thus suggesting increased drought resistance. Furthermore, long-term tree ring analyses from German sessile oak, European beech, and Norway spruce forests showed that, while spruce and oak show no difference in drought resistance when grown in either mixed or pure stands, beech trees are significantly more resistant in mixtures with spruce or oak (Pretzsch et al. 2013). This is believed to be caused by facilitative interaction effects such as hydraulic uplift of the deeper rooting system of oaks supplying water to the shallow roots of beech, and through a temporal stratification of stress response patterns, where 'isohydric' trees such as spruce close stomata early on and thus reduce further consumption of water, which is then made available to so-called 'anisohydric' species such as beech, that continue to photosynthesize until water is completely exhausted (Pretzsch et al. 2013; Forrester et al. 2016). Several studies support similar conclusions about facilitative interaction effects and drought resistance (e.g. Lebourgeois et al. 2013; Gazol et al. 2016).

In contrast to these findings, Grossiord et al. (2013) suggests the opposite to be the case in boreal forests, where mixed stands of Silver birch, Norway spruce, and Scots pine in a Finnish forest more

quickly exhausted available soil water during the dry-spell of 2006, leading to higher tree water stress levels than in their monospecific counterparts. As it seems, there might be no generalizable relationship between diversity and community-level drought stress (Grossiord et al. 2014), and the extent to which trees, when grown as heterogenous mixtures of different age classes and species, prove to be more drought resistant varies across regions and local conditions, with the same species benefitting when paired at some sites while showing no effect at others (Forrester et al. 2016).

Apart from species diversity, forest resilience is also closely linked to tree size and age, with larger trees often showing higher levels of delayed drought-induced tree-mortality, despite their more extensive rooting systems and thus improved water access; since resistance of passive water transport from the roots to the leaves is increased in tall trees, a higher xylem-tissue-to-leaf-ratio is needed for effective water use, severely hampering post-drought recovery once extensive xylem tissue damage has occurred, therefore making old and tall trees more susceptible to severe droughts (Trugman et al. 2018; Vanhellemont et al. 2019). On the other hand, uneven-aged forests can favor the relative growth of smaller trees during droughts, especially in stands with isohydric species, with smaller trees benefitting from the shading and the reduced water consumption of the taller trees, thus stabilizing overall stand growth (Pretzsch et al. 2018). In conclusion, whether Swedish old-growth forests benefit from facilitative processes, or suffer from increased competition for water resources, and the role that stand age and structure hereby play, currently constitutes a major research gap. Additionally, such systems stand in stark contrast to surrounding production forests whose management history, such as species selection of more-drought resistant phenotypes one the one hand, and forest drainage and thinning on the other hand, might severely alter drought resistance.

2.4. Signs of drought stress and their potential to be observed remotely

2.4.1 Reduced chlorophyll absorption

Vegetation indices (VIs) are designed to quantify vegetation information on a per pixel basis in a remotely sensed image (Chuvieco 2016). They are based on combinations of several satellite bands, making use of differences in the so-called ‘spectral signature’ of vegetation, that is, the variation in reflected radiation across different wavelengths (see Figure 3 for an example spectral signature of a coniferous species). VIs typically involve a band in the spectral region of strongest chlorophyll absorption, corresponding to the red (R) region (0.6-0.7µm), as well as one in the near-infrared (NIR) region (the whole region corresponding to about 0.7-1.2µm), in which most incoming radiation is reflected rather than being absorbed; combining these two spectral regions in a VI enhances the vegetation signal, as the contrast between NIR and R reflectance increases with the

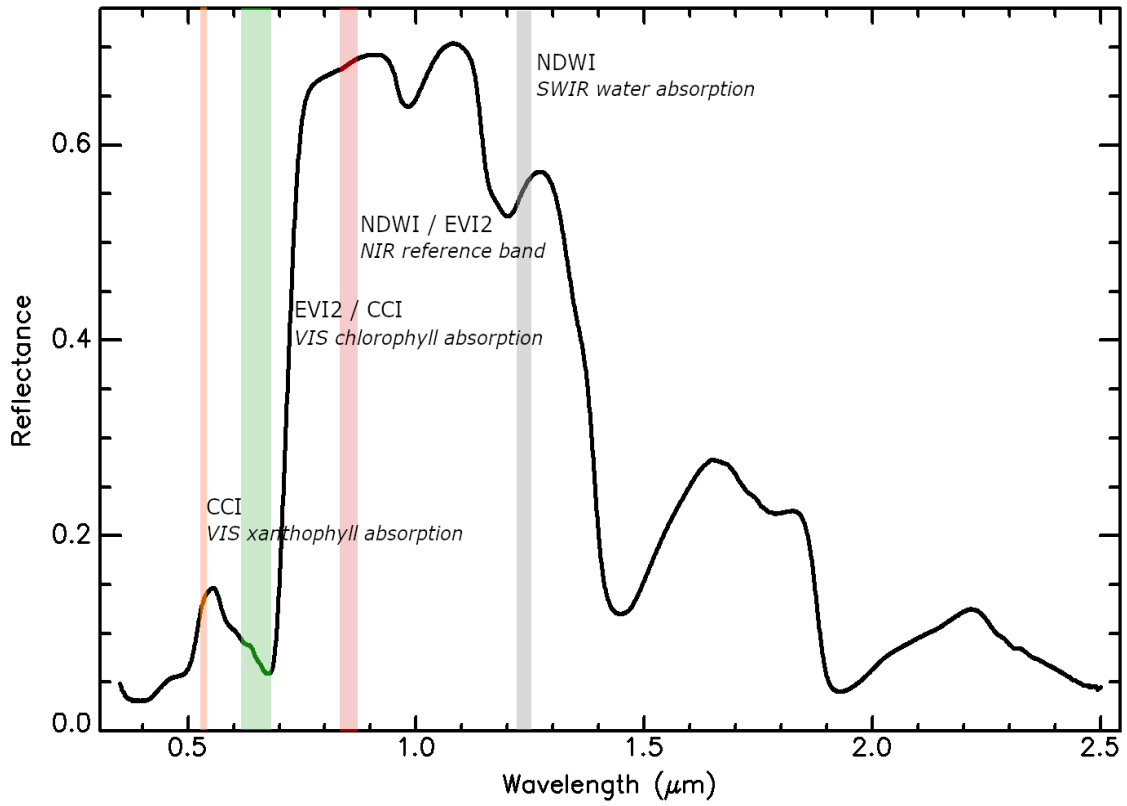

Figure 3: Spectral signature for needles of a coniferous tree species, showing regions of carotenoid, chlorophyll, and water absorption as utilized in the vegetation indices used in this study. Spectral signature retrieved and adapted from the USGS Spectral Library (Kokaly et al. 2017).

presence of vegetation in a pixel (Chuvieco 2016). Arguably the most well-known, ubiquitously applied VI is the Normalized Difference Vegetation Index (NDVI). NDVI is commonly used as a measure of general greenness and seasonal or interannual variations thereof, and as a proxy for biophysical variables such as GPP or biomass (Chuvieco 2016). However, NDVI does not scale linearly with biomass, leveling off over dense canopies. Therefore, an alternative VI, designed to minimize soil and aerosol influences and to solve the saturation problem over dense canopies, the so-called Enhanced Vegetation Index (EVI), is commonly used as an alternative to NDVI in high biomass regions. EVI has since been developed into a two-band version called EVI2 (Eq. 1), which no longer incorporates the blue band (Jiang et al. 2008).

$$EVI2 = 2.5 * \frac{\rho_{NIR} - \rho_R}{\rho_{NIR} + 2.4 * \rho_R + 1} \quad \text{Eq. 1}$$

Where ρ_{NIR} and ρ_R refer to satellite bands in the near-infrared, and red regions, respectively

When photosynthetic capacity is compromised, the leaves' absorption of solar radiation in the photosynthetically active wavelengths decreases, and comparatively more radiation is reflected instead, reducing the contrast between R and NIR (AghaKouchak et al. 2015). Both NDVI and EVI/EVI2 have been employed in various studies to quantify vegetation stress and drought impacts across Europe. For instance, Reinermann et al. (2019) used MODIS EVI time series to quantify spatiotemporal variability in drought impacts in Germany, investigating patterns of EVI anomaly for different land cover types and comparing the 2003 and 2018 droughts, concluding that, while 2018 spring phenology was above average, both years showed negative summer anomalies of similar magnitude, with grass and croplands the most affected. In contrast, no negative anomalies were found for forested areas for 2018, interpreted as forests either not being impacted due to their ability to reach deeper soil water, or showing a lag in response potentially only visible in the years to come. On a continental scale, Reichstein et al. (2007) investigated the 2003 drought impacts across Europe based on the MODIS FPAR product, whereby FPAR directly quantities the fraction of photosynthetically active radiation absorbed (fAPAR) rather than being a VI, but being based on the same principle of measuring reductions in chlorophyll absorption. The authors found FPAR anomalies to be strongest in autumn, two months after the maximum meteorological anomaly had occurred, pointing toward a delayed or cumulative vegetation response to drought stress. However, Reichstein et al. (2007) caution the use of FPAR and NDVI as a proxy of drought stress: for species with little control over stomatal closure, water stress can quickly lead to drying out and subsequent leaf yellowing; however, radiation received by a tree canopy might continue to be absorbed despite low leaf CO_2 concentrations, and then simply dissipated rather than used for carbon assimilation at initial stages of water stress; therefore, reflectance received by the satellite sensor will not necessarily be altered when discoloration or defoliation haven't occurred. In the context of this project, given the focus on detecting stress signals in largely coniferous forests, this highlights the potential of investigating alternatives to EVI2, whose performance in detecting lower levels of drought stress will likely be affected for the same reasons as stated by Reichstein et al. (2007).

2.4.2 Changes in carotenoid pigment pools

A VI which explicitly focuses on photosynthetic downregulation rather than changes in canopy chlorophyll content, is the so-called Photochemical Reflectance Index (PRI), formulated by Gamon et al. (1997): its original version is based on reflectance bands at 531nm and 570nm (Eq. 2), whereby the 531nm band is associated with changes in xanthophyll pigment absorption, and the 570nm region serves as an unaffected reference band. Xanthophylls are a subgroup of carotenoid pigments and are shown to be involved in the dissipation of excess energy in response to high irradiance, water deficit, or high temperature conditions: during such conditions, a short-term,

reversible photoprotective process is triggered, the so-called xanthophyll cycle, during which a group of three carotenoid pigments are interconverted, also known as 'xanthophyll de-epoxidation', causing decreased reflectance at 531nm (Gamon et al. 2016; Middleton et al. 2016). Changes in PRI are therefore in principle detectable on a diurnal timescale, with afternoon decreases observed at a Finnish coniferous forest site (Mottus et al. 2019). However, PRI is also influenced by longer-term changes in the overall ratio of carotenoid and chlorophyll pool sizes, caused by seasonality or longer-term stress events (Filella et al. 2009; Middleton et al. 2016). PRI is thus simultaneously tracking two different processes acting on different time scales, ranging from minutes to weeks.

$$PRI = \frac{\rho_{531} - \rho_{570}}{\rho_{531} + \rho_{570}} \quad \text{Eq. 2}$$

Where ρ_{531} and ρ_{570} refer to spectral regions (nm) of carotenoid and chlorophyll absorption

One challenge when using PRI is the availability of bands used in its original formulation, which are lacking for most satellite instruments, thus limiting the current applicability of PRI in satellite remote sensing. NASA's MODIS instrument happens to possess the necessary narrow band at wavelengths 526-536nm for xanthophyll absorption (band 11), albeit designed for ocean studies and not originally intended for use over land, coming at a coarse pixel resolution of 1km, and lacking the original 570nm reference band. Nevertheless, MODIS-derived PRI has successfully been linked to light use efficiency and GPP in various studies, in which the authors replaced the missing reference band with other bands, thus creating several new versions of the index (e.g. Drolet et al. 2005; Hernández-Clemente et al. 2011; Middleton et al. 2016). One of such PRI derivatives is the so-called Chlorophyll/Carotenoid Index (CCI, Eq. 3, see Figure 3), which uses MODIS band 1 as reference, centered around 645nm (Gamon et al. 2016).

$$CCI = \frac{\rho_{531} - \rho_{645}}{\rho_{531} + \rho_{645}} \quad \text{Eq. 3}$$

Where ρ_{531} and ρ_{645} refer to spectral regions (nm) of carotenoid and chlorophyll absorption

CCI has been shown to perform better in tracking changes in phenology at evergreen coniferous sites, where NDVI fails (Gamon et al. 2016), and has been proposed as a suitable VI to monitor both short and long-term water stress in coniferous forests not detected by chlorophyll-based indices (Middleton et al. 2016). Therefore, despite its coarse spatial resolution, MODIS-derived CCI offers an alternative approach to drought stress detection worth exploring.

2.4.3 Reduced canopy water content

Since drought stress is connected to changes in canopy water content, it can be detected through the use of water-sensitive RS indices (Dotzler et al. 2015). Water absorbs strongly in the shortwave infrared spectral region (SWIR, about 1.2-2.5µm), causing decreased reflectance across the SWIR region in moist leaves while having no direct effect on the NIR spectral region (Chuvieco 2016). One of several commonly used SWIR-based VIs is the Normalized Difference Water Index (NDWI, Eq. 4, Figure 3), which studies changes in water absorption at around 1241nm, alongside the unaffected NIR reference band; NDWI has been shown to retain sensitivity to leaf water content in dense canopies, thus being less prone to saturation with high leaf area index (LAI) values (Wang et al. 2008).

$$NDWI = \frac{\rho_{857} - \rho_{1241}}{\rho_{857} + \rho_{1241}} \quad \text{Eq. 4}$$

Where ρ_{857} and ρ_{1241} refer to regions (nm) of NIR and SWIR reflectance

MODIS-derived NDWI has for instance been used to study the effects of the 2003 drought on an ancient coniferous forest in the Pacific Northwest, whose annual fate as a net carbon sink or source, i.e. the directional sign of Net Ecosystem Exchange (NEE), has been observed to be largely connected to interannual precipitation differences. Variability in NDWI values were found to correspond to the spatiotemporal dynamics of NEE, while such variability was not detectable for NDVI (Cheng et al. 2007). However, water-sensitive VIs are confounded by soil moisture in sparser canopies, as well as by wet leaf surfaces shortly after a rainfall event, causing considerable noise in the signal of canopy water content.

2.5. The Google Earth Engine platform

Google Earth Engine (GEE) is a cloud-computing platform that enables free and easy user access, analysis, and visualization of various satellite and other geospatial datasets. The platform is based on a public data catalogue which hosts petabytes of preprocessed and therefore ready-to-use remote sensing imagery, such as the complete Sentinel-2, MODIS and Landsat surface reflectance data archives, which are continuously updated by newly ingested data (Gorelick et al. 2017). The data catalogue can be accessed through a GEE enabled Google account, and queries are created in the Integrated Development Environment 'Earth Engine Code Editor', which is based on a JavaScript application programming interface, optionally supplemented by a Python add-on. Queries written in Code Editor are composed of functions available in the Earth Engine Library, which support the

manipulation of object types such as images, points, and lines, thus enabling tasks commonly performed within a geographic information system, for instance, the band algebra needed to compute vegetation indices. Queries sent to the Earth Engine Server are handled through parallel processing, thus allowing the user to utilize Google's massive computational capacities (Gorelick et al. 2017).

Google Earth Engine has successfully been employed in a variety of different, large-scale scientific endeavors, such as for instance the quantification of annual global forest loss based on the Landsat collections (Hansen et al. 2013), boreal peatland mapping in Alberta through a combination of Sentinel-1, Sentinel-2, and SRTM DEM data (DeLancey et al. 2019), and automated cropland detection across the African continent through utilization of MODIS NDVI data (Xiong et al. 2017). In short, the GEE environment enables a fast exploration and manipulation of large datasets, thus opening an entirely new pathway to satellite data analysis. In the context of this project, it provides an ideal environment for comparatively straightforward computation and exploration of various vegetation index anomalies for different satellite sensors over multiple regions of interest, rather than constraining the project to an *a priori* choice of a suitable set of tiles to be downloaded.

3. Materials and methods

3.1. Forest maps used

3.1.1. Description of old-growth forest map and forest pairing

This project is based on an unpublished polygon map containing the boundaries of 391 Swedish primary forests, which represents a digitized and updated version of an extensive nationwide forest inventory map created in the 1980s (Naturvårdsverket 1982; see Ahlström et al. 2020 for further details). The map has since been complemented with additional detailed information collected on protection type and duration, as well as past human disturbance, based on which a ranking of pristineness level (ranging from 0-9, based on the framework established by Buchwald (2005)) was created (Ahlström and de Jong 2020 unpubl.). For the purpose of this study, only forests scoring five or higher (intact forests untouched for at least 60 years) were considered, leading to the exclusion of 43 complete forests and 147 forest parts. Figure 4A provides an overview of the final map used for further analysis; while the 348 old-growth forests are found scattered across Sweden, the largest continuous stretches are found in the North along the Norwegian border.

Subsequently, 15km buffer zones around all old-growth forest polygons were established, which represent the surrounding production forests, and, when linked to their respective old-growth

forests, form spatially proximate pairs (Figure 4B); this allows for a direct comparison of old-growth and production forests experiencing similar environmental conditions and atmospheric drought impacts during 2018. Any area of potential conservation value, such as nature reserves and key biotope areas, which are unlikely to present production forests, were excluded from the buffers (see Ahlström et al. 2020 for a full list of exclusions made). Furthermore, areas affected by forest fires in 2018 were excluded from both datasets, based on data obtained from the Swedish Forest Agency.

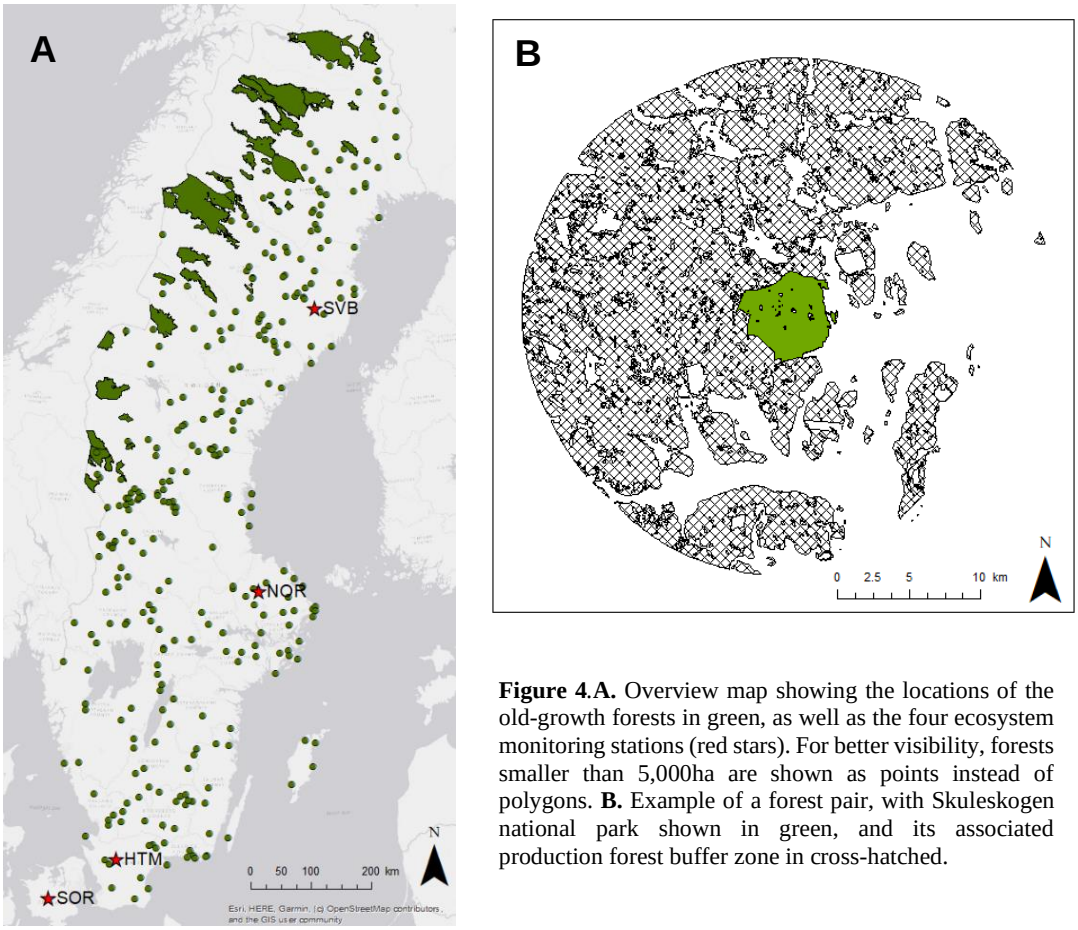

Figure 4.A. Overview map showing the locations of the old-growth forests in green, as well as the four ecosystem monitoring stations (red stars). For better visibility, forests smaller than 5,000ha are shown as points instead of polygons. **B.** Example of a forest pair, with Skuleskogen national park shown in green, and its associated production forest buffer zone in cross-hatched.

3.1.2. Further exclusions made during raster analysis

Non-forested areas and water bodies were excluded from any further raster analysis. For this, the national Swedish land cover map, generalized version 2.1 (‘Nationella Marktäckedata 2018’), supplied by the Swedish Environmental Protection Agency (© Naturvårdsverket 2019a), which is a 10m resolution raster map of Sweden containing information on 24 thematic classes, including 16 forest types, was reclassified to only include forests (land cover classes 111-117 and 121-127), and resampled (pixel majority) to the respective resolutions of the satellite imagery, so as to mask

out any pixels over non-forested land. Note that classes 118 and 128, constituting temporarily non-forested areas, were excluded based on a preliminary analysis showing that the most of those areas were in fact recently clear-cut, thus exhibiting the spectral signal of dry soil; however, these classes also include young forests with trees smaller than 5m, and therefore drought impacts on newly planted forest stands are not captured. The land cover map also contains a layer of 'productive forests', in this case referring to areas with environmental conditions in principle supporting an annual production of $1m^3$ timber (Naturvårdsverket 2019b). Based on this, non-productive areas were excluded, so as to allow for a more direct comparison of old-growth and production forests and therefore the impact of forest management, since old-growth forests tend to be found in environments less favorable for timber production. Moreover, many of the non-productive areas, when investigated on aerial imagery, contained sparse stands with a disproportionally large fraction of exposed understory. For the remainder of this project, the Sweden-wide productive forest layer contained in the land cover map will be referred to as 'productive forest land' so as to avoid confusion with the established 15km buffer zones defined as managed 'production forest'.

3.2. GPP and drought indicator retrieval and treatment

3.2.1. Flux tower site descriptions and GPP retrieval

In order to test the whether the VIs capture anomalies of gross primary production (GPP) over a diverse range of different forest types (Research question 1), the four ecosystem monitoring stations Soroe (SOR), Hyltemossa (HTM), Norunda (NOR), and Svarteberget (SVB) were chosen as representative sites. Soroe, although being located in Denmark, was included as it is one of the few Scandinavian monitoring sites with deciduous forest; see Table 1 for a more detailed site description and Figure 4A for their location.

Flux tower measurements were retrieved from the 'Drought-2018 FLUXNET product', a newly released data set by the Integrated Carbon Observation System Network as well as the Drought-2018 working group, freely available for 52 monitoring stations (ICOS 2020). The product contains Level-2 processed (i.e. quality-controlled and published) half-hourly CO_2 measurements for the year 2018, as well as several preceding years, with the precise time period covered varying across monitoring sites. After downloading, the GPP dataset based on the day-time partitioning method (GPP_DT_VUT_REF) was extracted for further use, night-time zero values were excluded, half-hourly fluxes were aggregated to daily values, and units were converted from umolCO2 m^{-2} s^{-1} to gC m^{-2} d^{-1}. Lastly, the daily average GPP data was filtered for the months April-September to only include growing season months.

Table 1: Overview of the four monitoring stations, dominant vegetation type, and SPI-3 drought severity

Site name	Coordinates	Time period	Vegetation	Lowest SPI-3
Soroe	55°29'09.1"N 11°38'40.7"E	2008-2018,	Mature beech forest	-3.0 (July)
Hyltemossa	56°05'52.0"N 13°25'07.9"E	2015-2018	Planted 1983, thinned 2009 and 2013. Norway spruce dominant, small fraction of birch and Scots pine. Tree height 19m.	-3.3 (July)
Norunda	60°05'11.4"N 17°28'46.2"E	2014-2018	Managed for 200y, drained 100ya. Norway spruce and Scots pine dominant, small fraction of birch. Varying tree ages of 110-60y, dominating tree height 25m.	-1.4 (June)
Svarteberget	64°15'22.0"N 19°46'28.2"E	2014-2018, 2017 missing	60% Scots pine, 40% Norway spruce. 100y old, tree height 20m.	-3.2 (July)

3.2.2. SPI-3 and scPDSI retrieval

The Standardized Precipitation Index (SPI) is a drought indicator for meteorological droughts, measuring local precipitation anomalies based on a comparison of monthly precipitation (interpolated to 0.25° grid data for Europe) with the historic precipitation record (1981-2010); SPI itself can be calculated for different accumulation periods, thus representing impacts occurring at varying time scales (European Commission 2020). Since the drought in Sweden was preceded by an already dry spring, SPI-3 based on an accumulation period of three months and representing reduced soil moisture and diminished stream flow, was chosen as a suitable index; time series for point locations of interest were obtained through the data portal of the European Drought Observatory (CEMS 2019). The scores correspond to standard deviations and can be interpreted as +1/-1 being near normal, -1/-1.5 moderately dry, -1.5/-2 severely dry, and values smaller than -2 as extremely dry (European Commission 2020). Since SPI-3 is currently not available as a ready-made gridded dataset, raster data for the self-calibrating Palmer Drought Severity Index (scPDSI) was retrieved for the months July – September 2018 (Barichivich et al. 2018). In contrast to SPI, scPDSI additionally incorporates temperature data and a primitive water balance model, thus also accounting for the effect of evapotranspiration on water stress, but coming at a coarser resolution of 0.5° (Wells et al. 2004). July-September per-pixel mean values were computed and projected to SWEREF99 TM, and values were extracted for all forests.

3.3. Computations of vegetation indices and Z-scores

3.3.1. VI timeseries computations in GEE and comparison with GPP data

Based on the considerations of spectral, temporal, and spatial scale as elaborated on in Section 2.4, the MODIS instrument aboard NASA's sun-synchronous Aqua satellite, currently providing the only freely available dataset enabling a quantification of the carotenoid-based index CCI, was chosen. With a daily, early-afternoon overpass time in Sweden and a record dating back to 2002, MODIS Aqua furthermore provides the ideal temporal resolution; however, depending on the bands used, spatial resolution ranges from 250m to 1km.

Furthermore, data by the TM/ETM+/OLI instruments aboard the Landsat 5, 7, and 8 platforms by NASA/USGS were extracted, due to their high spatial resolution of 30m, albeit with an individual revisit time of 16 days, making data loss due to cloud cover an important issue. ESA's Sentinel-2 dataset was explored as well, but its time in orbit is too short to establish a meaningful pre-drought baseline in the context of this project (atmospherically corrected data is only being operationally ingested since March 2017).

All data extraction and VI computations were executed in Google Earth Engine. For MODIS, daily surface-level reflectance (L2G) Image Collections MYD09GQ, MYD09GA and MYDOCGA were loaded and merged, whereby the first collection contains bands 1 and 2 at a 250m resolution, the second bands 1-7 at 500m, as well as cloud and viewing geometry information, and the third contains the band 11 needed for CCI computation. Sensor zenith angles larger than 45 degrees were excluded to avoid pixel distortion and further degradation of spatial resolution. Clouds and cloud shadows were filtered based on quality information held in the 'state_1km' band.

Daily EVI2, NDWI, and CCI values were computed for the years 2008-2018. In order to investigate whether the VIs captured the GPP anomalies observed at the flux stations (Research question 1), single-pixel time series data corresponding to the point locations of the flux towers were extracted and downloaded. Note that a considerable amount of past research has focused on correct RS data representation of the spatial flux tower footprint, which dynamically changes in size depending on prevailing wind conditions. However, since accurate GPP modeling is not the objective of this project and MODIS data is already quite coarse-resolution, single-pixel timeseries were instead deemed a better suited way of detecting the presence of temporal dynamics, rather than averaging over a larger area, hereby following a similar line of reasoning as by Cai et al. (2017). Lastly, cloud filtering based on the built-in quality band was found insufficient for complete cloud removal, and therefore an additional, heuristic data filtering method was developed: tiles corresponding to dates of sudden up- or downward spikes in the time series data were visualized as RGB color composites, and through this, individual thresholds based on observable residual cloud (shadows) were determined: for EVI2 values smaller than 0.15 (unrealistically low for forests during the growing

season) were excluded, for NDWI, values smaller than -0.2 (unrealistically dry), and for CCI, values larger than 1 (outside the possible range of the index), as well as values smaller than -0.4 (extreme stress levels not observed in other literature and associated with clouds) were additionally filtered out.

For Landsat, surface reflectance Tier 1 collections 5, 7, and 8 were loaded, and clouds and cloud shadows were filtered out based on the respective 'pixel_qa' bands. EVI2 was computed and Landsat 5 and 8 were intercalibrated to match the Landsat 7 values (Tian 2020, unpubl.), and despiked using the same thresholding method as described above. Lastly, in the context of GPP anomaly detection, EVI2 values were averaged over a buffer zone with a diameter of 250m to correspond to a footprint size resembling that of MODIS EVI2 to allow for better comparison. While Landsat does contain the necessary bands to compute NDWI, its temporal resolution was deemed to coarse to enable a meaningful interpretation of the index, which changes more dynamically than EVI2. See Table 2 for a summary of the VIs retrieved in GEE and the bands used for computation.

Table 2: Summary of vegetation indices calculated, datasets and bands used, their associated spatial and temporal resolutions, and data filtering in GEE.

VI	Dataset	Used bands	Spatial res.	Revisit	Data filtering
EVI2	MYD09GQ	B1, B2	250m	daily	Filtering based on QC_250m and state_1km, sensor zenith angles >45°, despiking (EVI2 <0.15)
NDWI	MYD09GA	B2, B5	500m	daily	Filtering based on state_1km, sensor zenith angles >45°, despiking (NDWI < - 0.2)
CCI	MYD09GA, MYDOCGA	B1, B11	1km	daily	Filtering based on state_1km, sensor zenith angles >45°, despiking (CCI <-0.4 and >1)
EVI2	LANDSAT/LT05/C01/T1_SR, LANDSAT/LE07/C01/T1_SR, LANDSAT/LC08/C01/T1_SR	B3, B4 (Landsat 5, 7), B4, B5 (Landsat 8)	30m	16 days per satellite	Calibration to Landsat 7, filtering based on pixel_qa, despiking (EVI2 <0.15), for Q1 averaging to 250m resolution

Subsequently, all further analysis was executed in *R* version 3.6.2 (R Development Core Team 2013). VI and GPP time series were aggregated to 14-day median value composites, starting with DOY 92 (weeks 14-39 in 2018). This was done to enhance the signal developing over a longer time scale, and to smooth out short-term daily variations in the VI data caused by residual noise of low-

quality data that was not caught by the quality filter, as well as noise such as caused by differing viewing angles. Note that a common choice of compositing method is the use of maximum – rather than median – value composites, with the assumption that lower values tend to be associated with residual clouds (e.g. Middleton et al. 2016); however, since this also holds for drought impacts, the maximum-compositing approach was found to be less suitable as it would weaken short-term signals, and median-value composites therefore constitute a suitable tradeoff. 2018 median values were computed for all VI and GPP data, and compared to their respective baseline median, 5th-, 25th-, 75th-, and 95th-percentiles, so as to highlight the extent to which the 2018 observations deviate from the long-term site conditions. 2008-2017 was chosen as a 10-year baseline period for the VIs so as to exclude damage associated with the 2005 windstorm, as well as the 2006 heatwave; however, the Fluxnet Drought-2018 product did not contain the same length of records for all stations, and thus differing baselines were established based on data availability (Table 1).

3.3.2. Z-score calculations and investigation of effect of spatial scale

Median-value Z-scores for the month of August for all VIs for Skuleskogen national park (63°07'N 18°30'E, SPI-3 value in August = -1.41), a test site representative of the typically hilly and fragmented landscape encountered in large parts of Sweden (Figure 1 in section 2.1), were computed, so as to compare the effect of the choice of spatial resolution on observed drought impacts (Research question 1 continued). 2008-2017 values were used as a baseline to compute per-pixel long-term VI means and standard deviations. Z-scores quantify how many standard deviations the 2018 remotely sensed VI values were above or below the baseline mean, thus representing a standard score that allows for easier quantification of drought impacts across different vegetation types (Eq. 5). See Appendix A for an example script in GEE.

$$Z\text{-}score = \frac{VI_{2018} - VI_{mean}}{VI_{SD}} \quad \text{Eq. 5}$$

Where VI_{2018}, VI_{mean}, and VI_{SD} refer to the VI values computed for 2018, and the baseline (2008-2017) mean and standard deviation, respectively

3.4. Upscaling of methodology to old-growth and production forests

3.4.1. Sweden-wide Z-score map and division into soil moisture classes

Based on the results of the first part of this project, the use of Landsat EVI2 Z-scores was chosen as the most suitable method to study drought impacts on Swedish old-growth and production forests (Research question 1). To answer research question 2, Sweden was split into four sections for which

EVI2 Z-scores were computed separately in GEE, and the resulting raster data were downloaded, merged, projected to the national Swedish reference system (SWEREF99 TM), and all non-forested areas were masked out. These steps and all map creations were executed in ArcGIS Desktop 10.5.1. While this was initially performed for August Z-scores, this resulted in areas of central Sweden either lacking data due to complete cloud filtering or exhibiting unrealistically low Z-scores (-9 and lower) associated with spurious cloud shadows as the only available, falsely nonfiltered, monthly data. Therefore, median Z-scores for the summer months were examined separately, and based on this, seasonal Z-scores based on July-September median composites were recomputed; June was found to be least impacted and thus excluded.

Since a preliminary analysis revealed topographical differences in drought impacts, the Z-score map was split into five separate soil moisture (SM) classes, based on a topographical SM index raster which quantifies theoretical soil moisture through a combination of depth-to-water and topographical wetness index (TWI); the 10m-resolution index is unitless and ranges from 0-240 (Naturvårdsverket 2019c). The SM raster was resampled to the resolution of Landsat (bilinear interpolation) and reclassified into five classes, subsequently referred to as SM classes 1 (values 0-50, driest) to 5 (values 200-240, wettest); this resulted in five separate, final Z-score raster datasets. SM classes were treated separately because 1) impacts across different soil moisture classes were found to be bidirectional, i.e. wetter classes showed positive anomalies, while drier classes were negatively impacted, necessitating separation to avoid a cancelling of the signal, and 2) the occurrence of old-growth forests is likely to systematically coincide with moisture regimes less favorable for timber production, thus introducing a bias in the data that needs to be accounted for.

3.4.2. Paired analysis of drought resistance and overall spatial distribution

The five Z-score raster datasets were used to extract mean scores for all individual old-growth and production forests per soil moisture class, and the results were plotted as paired scatterplots to illustrate the relative difference in drought impacts between individual pairs. To test whether old-growth forests are associated with greater Z-scores than their surrounding production forests, a one-tailed Wilcoxon signed-rank test (significance level $\alpha = 0.05$) was performed for each SM class separately. A nonparametric test was chosen, because the Z-score differences of the forest pairs (old-growth – production) display a negatively skewed distribution, and only pairs in SM class 5 were found normally distributed (Shapiro-Wilk test, significance level $\alpha = 0.05$).

Moreover, in order to illustrate the overall spatial distribution of Z-score differences, a single combined score of all SM classes was calculated for each forest pair, whereby per-class Z-score differences were normalized by the overall frequency of occurrence of the respective SM class across all Swedish productive forest land.

3.4.3. Analysis of potential explanatory variables

In order to identify potential drivers of the observed differences in drought impacts, the effects of meteorological drought severity (scPDSI), latitude, elevation (m), slope (°), and stand age (years) on EVI2 Z-scores were tested for through partial linear regression. This was done for those forest pairs belonging to soil moisture (SM) class 2, the most frequent SM class across Swedish productive forest land. Effects of the variables on old-growth and production forest Z-scores were first tested for separately, and subsequently the effect of within-pair differences (old-growth – production) in elevation, slope, and stand age on Z-score differences was analyzed. Data were retrieved from a 50m-resolution digital elevation model (DEM) (Lantmäteriet 2009) and a 10m-resolution stand age raster (SLU 2010), which were subjected to the same procedure as described in sections 3.4.1 and 3.4.2 so as to obtain per-forest mean values. Since no initial relationship was found between those variables and the forest pairs when analyzed as a single dataset (n = 344, 3 pairs were excluded due to data gaps in the age raster), the data was instead split into three broad vegetation zones (Boreo-Nemoral, Boreal, and North Boreal / Alpine) and relationships were analyzed separately for each vegetation zone; boundaries of the zones were retrieved through digitization of the map provided by KSLA (2015).

Furthermore, within-pair differences in stand-age, elevation, and slope of the 15 largest positive (EVI2 Z-scores old-growth >> production) and negative (EVI2 Z-scores old-growth << production) outliers were analyzed with boxplots, and their significance was tested for with two-tailed Wilcoxon signed-rank tests (significance level $\alpha = 0.05$). Lastly, differences in species were also analyzed for these outliers. To do so, the land-cover raster (see section 3.1.2) was reclassified into five broad forest types: purely deciduous (including hardwood species), mixed forest (both coniferous and deciduous present), mixed coniferous, spruce, and pine. Subsequently, differences in fractions of each forest type were calculated for the area covering SM class 2 of each forest pair.

4. Results

4.1. Suitability of vegetation indices to study drought impacts

4.1.1. Temporal anomalies of precipitation, GPP and VIs

All four ecosystem monitoring stations, irrespective of their location, experienced prolonged summer precipitation deficits, with 2018 SPI-3 index values generally being lowest in the months June and July, followed by a slightly less impacted August (Figures 5A – 8A). During those months, drought severity ranged from ‘extremely dry’ for Soroe, Hyltemossa, and Svarteberget, to

‘moderately dry’ in Norunda. However, temporal GPP anomalies over time show contrasting responses, with the two southernmost sites (Soroe, Hyltemossa) exhibiting strong negative anomalies, while the central (Norunda) and northern (Svarteberget) sites show increased and near-normal GPP rates, respectively (Figures 5B – 8B), despite local precipitation deficits. At the two negatively impacted stations, the steep drop in GPP occurred around mid-June and lasted throughout the summer until the beginning of September, with the lowest GPP rates in the beginning of July in Hyltemossa (reduction by 62% from baseline median) and end of July in Soroe (reduction by 32% from baseline median). Moreover, all four stations show increased spring GPP rates in May and the beginning of June, with the most notable and sustained positive spring anomaly occurring in Soroe (mid-May increase by 25% from baseline median).

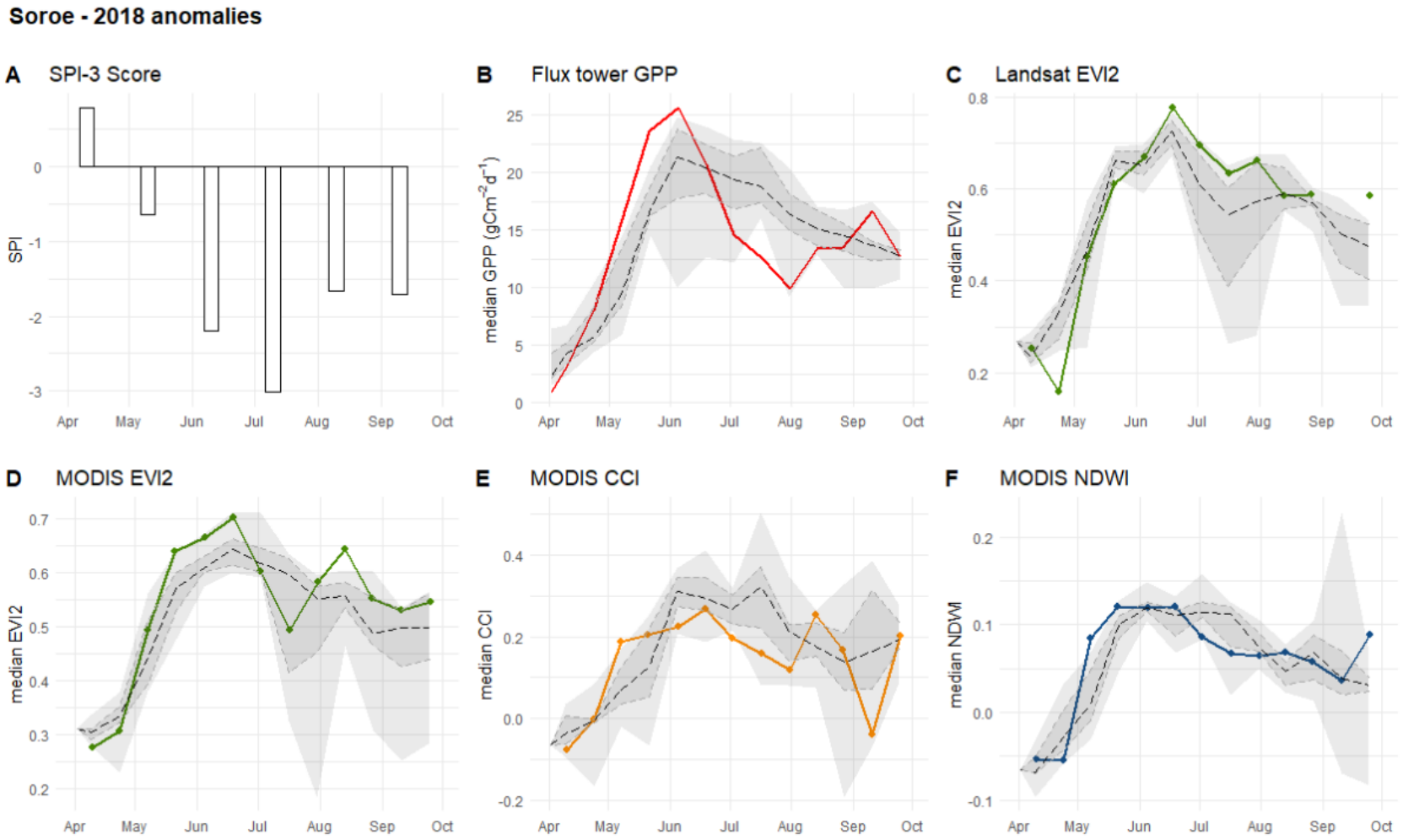

Figure 5: Precipitation, GPP, and VI anomalies in Soroe, showing **A**. SPI-3 scores, and 14-day median values of **B.** measured GPP, **C.** Landsat EVI2, **D.** MODIS EVI2 **E.** MODIS CCI, and **F.** MODIS NDWI. Dashed lines, dark, and light grey envelopes depict baseline median, 25/75-, and 05/95-percentile values respectively, where the GPP baseline refers to the period available in the Drought-2018 product (2008-2017), and the VI baselines to the years 2008-2017.

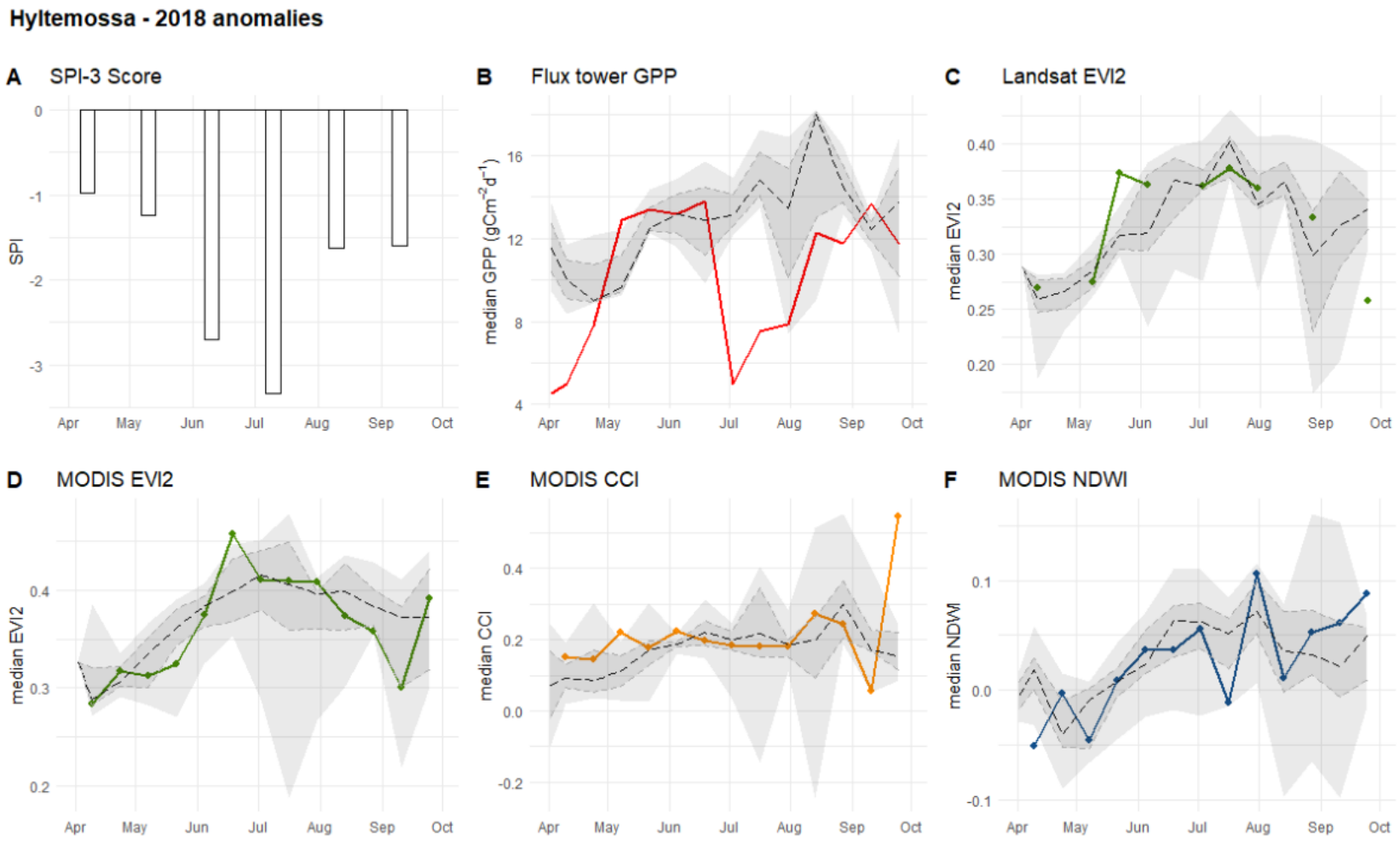

Figure 6: Precipitation, GPP, and VI anomalies in Hyltemossa, showing **A**. SPI-3 scores, and 14-day median values of **B.** measured GPP, **C.** Landsat EVI2, **D.** MODIS EVI2 **E.** MODIS CCI, and **F.** MODIS NDWI. Dashed lines, dark, and light grey envelopes depict baseline median, 25/75-, and 05/75-percentile values respectively, where the GPP baseline refers to the period available in the Drought-2018 product (2015-2017), and the VI baselines to the years 2008-2017.

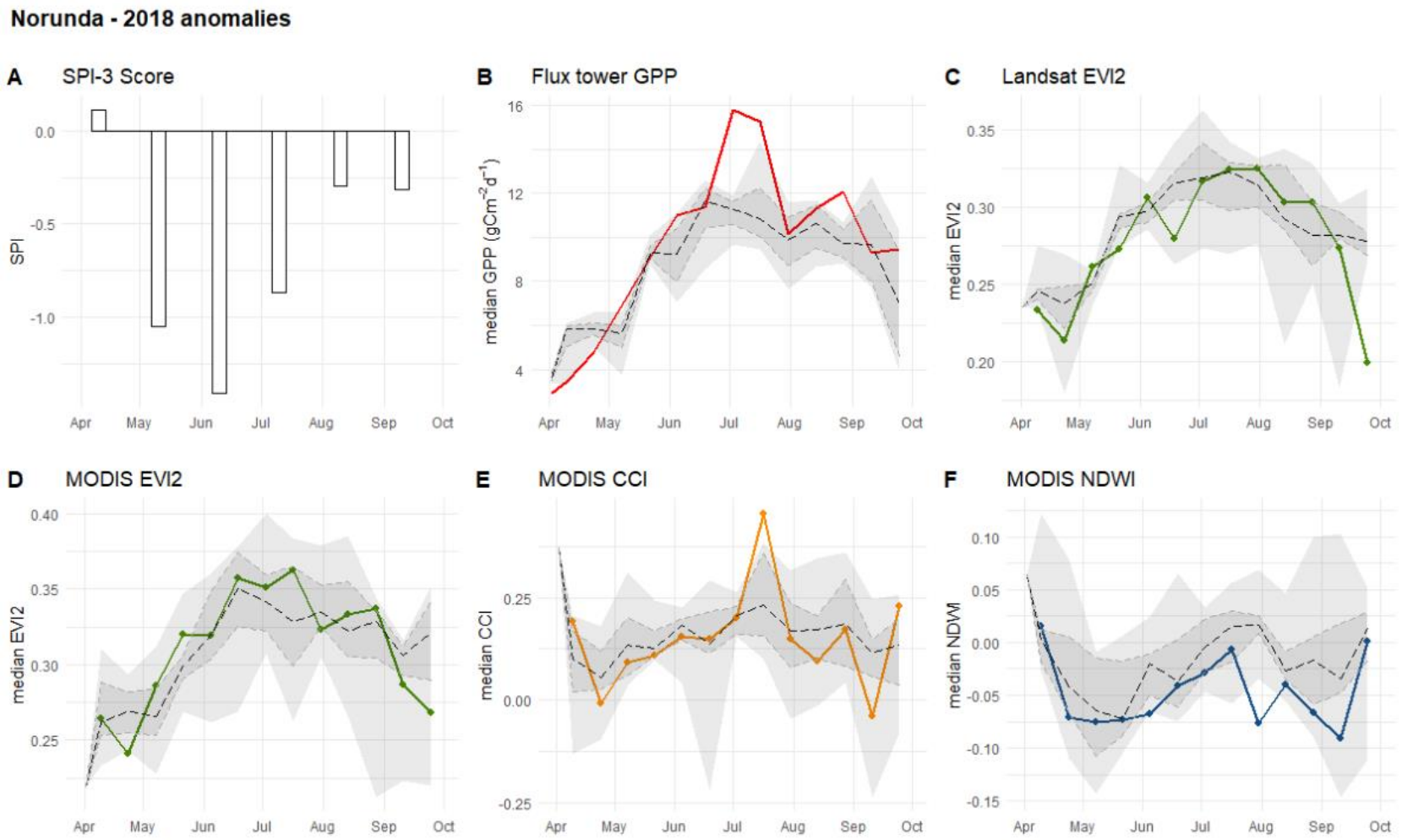

Figure 7: Precipitation, GPP, and VI anomalies in Norunda, showing **A**. SPI-3 scores, and 14-day median values of **B.** measured GPP, **C.** Landsat EVI2, **D.** MODIS EVI2 **E.** MODIS CCI, and **F.** MODIS NDWI. Dashed lines, dark, and light grey envelopes depict baseline median, 25/75-, and 05/95-percentile values respectively, where the GPP baseline refers to the period available in the Drought-2018 product (2014-2017), and the VI baselines to the years 2008-2017.

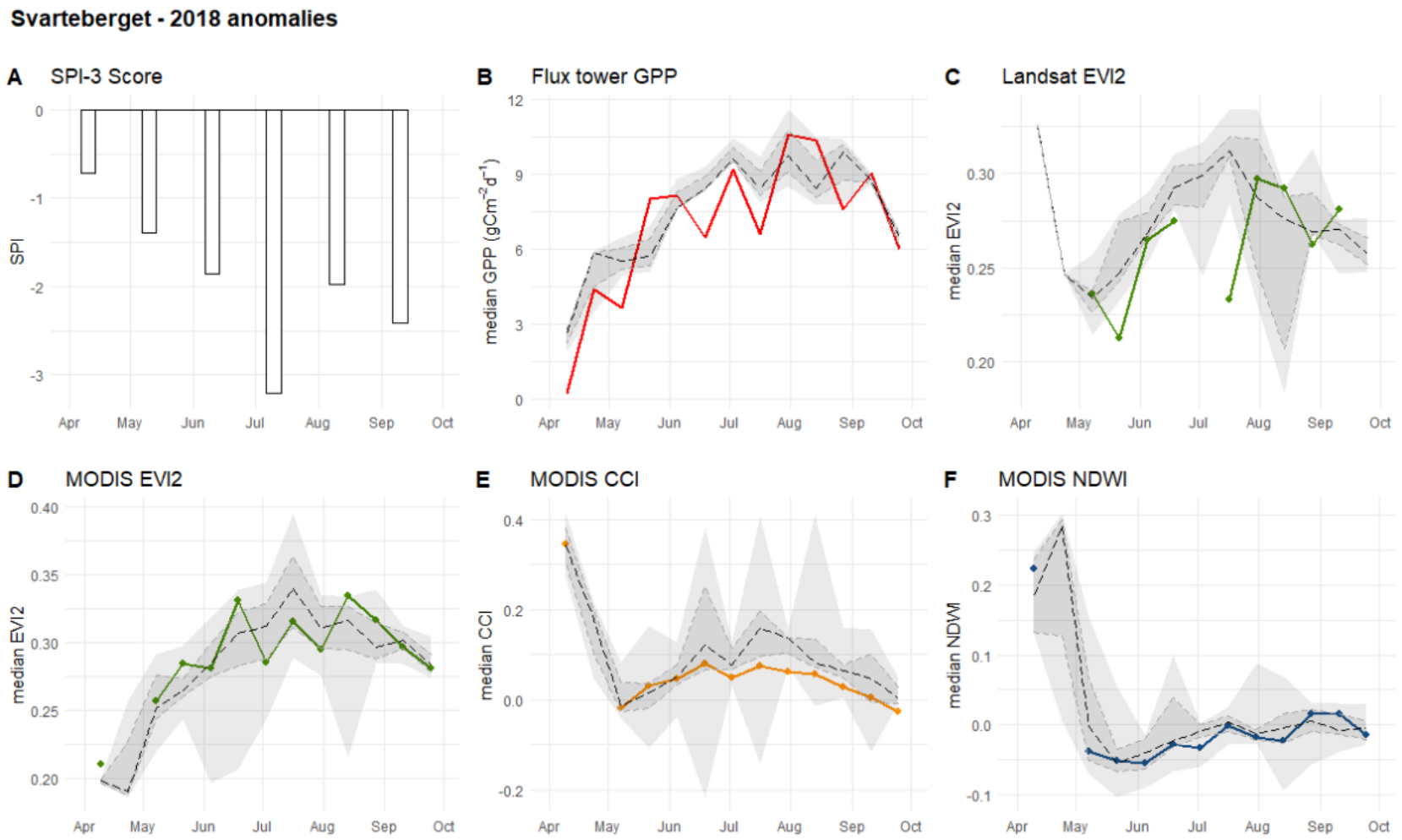

Figure 8: Precipitation, GPP, and VI anomalies in Svarteberget, showing **A**. SPI-3 scores, and 14-day median values of **B.** measured GPP, **C.** Landsat EVI2, **D.** MODIS EVI2 **E.** MODIS CCI, and **F.** MODIS NDWI. Dashed lines, dark, and light grey envelopes depict baseline median, 25/75-, and 05/95-percentile values respectively, where the GPP baseline refers to the period available in the Drought-2018 product (2014-2016), and the VI baselines to the years 2008-2017.

None of the four tested vegetation indices (Landsat EVI2, MODIS EVI2, MODIS CCI, MODIS NDWI) reliably captures the observed GPP anomalies. In Soroe, Landsat EVI2 displays peak values in greenness, subsequently followed by a decrease, in line with the observed occurrence of the peak in GPP rate (Figure 5C); it also successfully captures the positive spring anomaly in Hyltemossa (Figure 6C), as well as the short-term drops in GPP rates measured at the Svarteberget site (Figure 8C). However, the full magnitude of GPP anomalies throughout the most-severely affected months is not captured: in Soroe and Hyltemossa, Landsat EVI2 anomalies remain elevated compared to the respective baseline periods, despite strong reductions in GPP values, and the positive GPP anomalies in Norunda are not captured at all. Moreover, Landsat's revisit time (16 days) leads to periods of data gaps in Hyltemossa and Svarteberget, where low-quality data was filtered out.

MODIS EVI2 alleviates the latter problem of data gaps, due to the satellite's daily revisit time. Furthermore, in contrast to Landsat, it not only captures the occurrence of the peak GPP rates in Soroe, but also the preceding positive spring anomalies, as well as the negative GPP anomaly in July; however, the latter negative anomaly in the vegetation index is still lying well within the natural variability of the baseline variation (Figure 5D). Likewise, temporal dynamics in Norunda and Svarteberget are well captured: MODIS EVI2 displays positive anomalies in mid-July and end-August in Norunda, as would be expected based on the GPP values (Figure 7D), and the same holds for the dynamic fluctuations as observed in Svarteberget (Figure 8D), thus performing better than its Landsat equivalent at those sites. However, the strong negative GPP anomalies observed in Hyltemossa are captured neither by Landsat nor MODIS EVI2 (Figure 6D).

CCI captures the positive spring and negative summer anomalies in Soroe well (Figure 5E), and it replicates the peak of positive GPP anomalies in Norunda (Figure 7E). However, unlike the chlorophyll-based indices, it does not capture the short-term fluctuations in Svarteberget, but instead suggests constant CCI levels below the baseline median and thus prolonged, slightly increased stress levels (Figure 8E). For Hyltemossa, CCI values closely follow the baseline median, thus not capturing the negative GPP anomalies at all (Figure 6E). Moreover, the spikes in the baseline $05^{th}/95^{th}$-percentiles, as is for instance the case for Svarteberget, illustrate a high short-term variability in CCI values; note that carotenoid pigment pool sizes are influenced by different processes acting on different time scales (see section 2.4.2), making the establishment of a meaningful baseline less straightforward, as short-term, elevated stress-levels are not controlled for.

Lastly, temporal NDWI dynamics follow the pattern in GPP rates in Soroe well (Figure 5F). However, values for Norunda are constantly below the baseline median (Figure 7F), suggesting a drier canopy than what would be expected based on the elevated GPP rates. For Svarteberget, no

noticeable change from the baseline median is observed (Figure 8F), and neither is the prolonged negative GPP anomaly in Hyltemossa captured (Figure 6F).

In short, none of the indices capture GPP dynamics at the Hyltemossa site; in Soroe, CCI and NDWI perform best in capturing both elevated spring values, followed by the subsequent prolonged drop, which is captured to a lesser degree by MODIS EVI2 and not at all by Landsat EVI2. In Norunda, positive anomalies are captured by MODIS EVI2 and CCI, but not by Landsat EVI2 and NDWI. At the Svarteberget site, MODIS EVI2 and NDWI perform best in capturing temporal dynamics, while MODIS CCI suggests constant stress levels, and Landsat EVI2 suffers from too many data gaps to make the signal readily interpretable. Thus, neither of the VIs can clearly be related to GPP anomalies; subsequent use and interpretation of the VIs should therefore be done with the expectation that local discrepancies between drought stress as suggested by the remotely sensed data and what is occurring on the physiological level, are likely.

4.1.2. Effect of spatial scale

Skuleskogen national park, chosen as a test site, is characterized by a rough topography, with elevations ranging from sea level along the park's eastern shoreline, to 280m in the northwest, with rocky peaks interspersed by deep ravines; consequently, topographical soil moisture varies widely across the full spectrum of index values, with the wettest soils found within a network of narrow valleys, and increasingly drier soils along the slopes and on hilltops (Figure 9A). Vegetation varies accordingly, with large parts of the wettest areas dominated by Norway spruce, while the drier areas are preferentially vegetated by mixed stands or Scots pine (Figure 9B).

Landsat EVI2 Z-scores, coming at a resolution of 30m, clearly mirror this in the distribution of drought impacts, with a mean value of -0.49 ± 1.2 (mean ± SD), and positive values occurring in the areas expected to be wettest, while the most negatively impacted areas are found along dry slopes (Figure 9C). Note that the SPI-3 score for August (-1.41) in Skuleskogen suggests moderately dry conditions, which are of similar magnitude as the precipitation anomalies measured at the Norunda site (section 4.1.1).

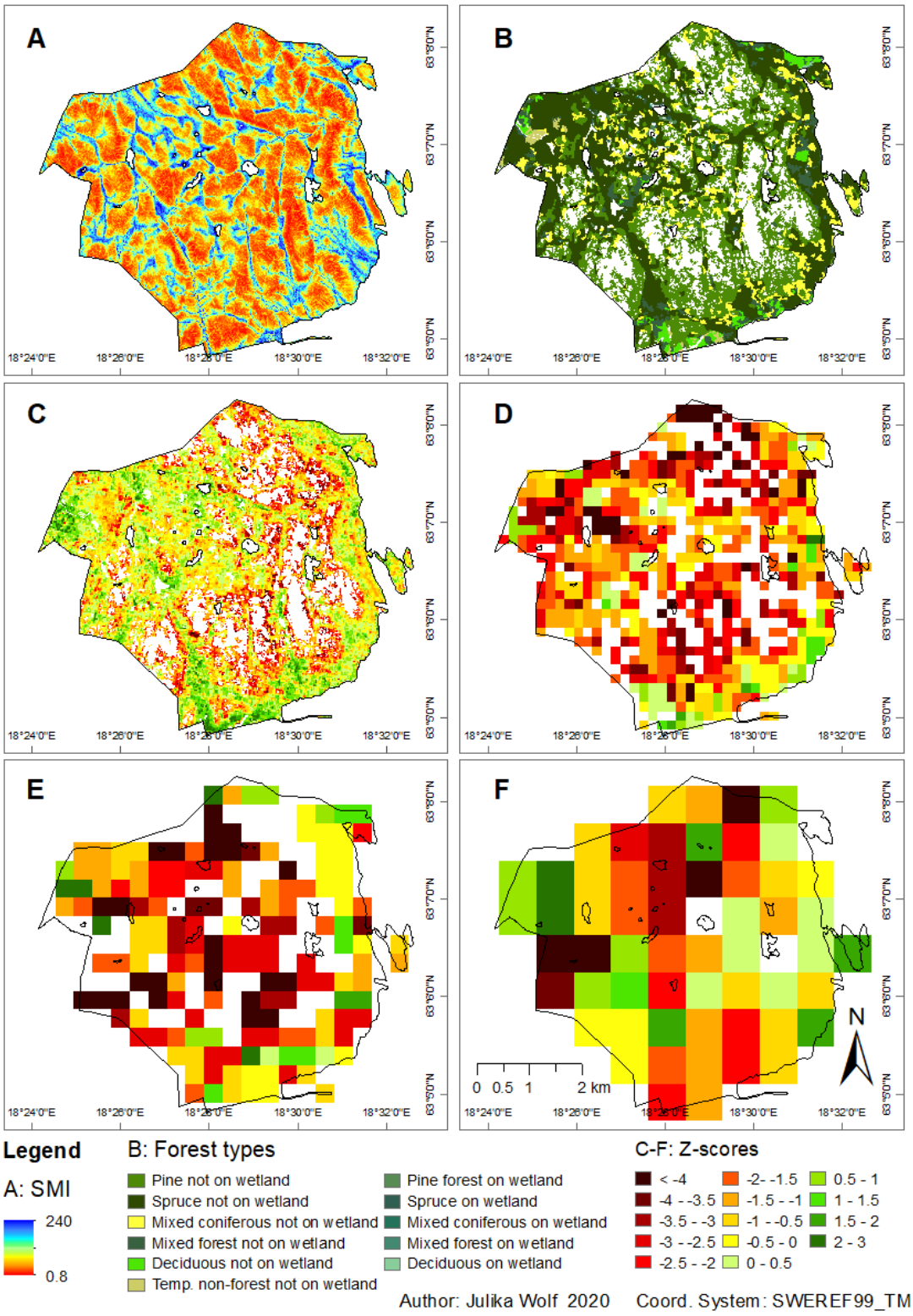

Figure 9: Comparison of spatial patterns of VI anomalies associated with increasingly degraded spatial resolution across the topographically varied national park Skuleskogen. **A.** Soil Moisture Index, **B.** Landcover map showing the distribution of pine, spruce, mixed coniferous, and deciduous forest types, and Z-scores of 2018 August median VI values when compared to the 2008-2017 baseline, non-forested areas excluded, for **C.** Landsat EVI2, **D.** MODIS EVI2, **E.** MODIS NDWI, and **F.** MODIS CCI

The pattern of drought impacts is increasingly degraded with the decreasing spatial resolution associated with the other three vegetation indices, MODIS EVI2 (250m), NDWI (500m), and CCI (1km). While MODIS EVI2 does reflect a greening along the lowest elevations near the park borders, it does not capture the local greening in the ravines and in the wetlands in the central parts of the park (Figure 9D); furthermore, overall drought impacts (-1.72 ± 1.53, mean ± SD) are more negative than those measured by Landsat EVI2. Lastly, the further degraded resolution of NDWI and CCI make any meaningful interpretation of their respective Z-scores close to impossible, since the majority of pixels are 'mixels' that contain areas of rocky peaks, as well as different forest types and moisture classes (Figures 9E and 9F).

Based on this, it was decided 1) to execute the remainder of the project with Landsat EVI2, as it currently constitutes the only available vegetation index with a long enough time record to establish a meaningful baseline and a spatial resolution that is deemed appropriate to study drought impacts across topographical differences, and furthermore that 2) topographical soil moisture differences need to be explicitly treated, which is seldomly done in remote-sensing drought impact studies.

4.2. Drought resistance in old-growth and production forests

4.2.1. Analysis of all forest pairs and different moisture classes

The pairwise comparison of old-growth and production forests shows that, on average, old-growth forests are associated with significantly higher EVI2 Z-scores during the 2018 drought than their surrounding production forests (one-tailed Wilcoxon signed-rank test, $p < 0.001$). While this finding holds true irrespective of soil moisture (SM) class, mean differences in EVI2 Z-scores (old-growth – production) tend to decrease with increasing soil moisture, being +0.155 for the driest, and +0.110 for the wettest SM class. More precisely, 65.1%, 63.1%, 63.1%, 58.7%, and 60.6% of old-growth forests showed higher Z-scores (Z-score difference > 0) than their productive counterparts in the five SM classes, respectively. When only considering those forests associated with considerably higher Z-score differences (>0.5), the numbers amount to 22.6%, 20.7%, 18.7%, 17.5%, and 16.3% respectively. In contrast, only 10.9%, 9.8%, 9.2%, 10.8%, and 8.1% were associated with considerably more negative differences (< -0.5), where old-growth forests scored lower Z-scores than their productive counterparts. Figure 10 provides an overview of the Z-score distribution per forest type and moisture class.

Most forests showed negative drought impacts (i.e. negative Z-scores), while some forests experienced greening (i.e. positive Z-scores); the degree to which this happens is related to soil moisture; in the driest SM class, 80.4% of the old-growth forests and 94.7% of the production forests were negatively impacted, while the numbers amounted to 54.4% and 66.3% in the wettest

SM class, highlighting the importance of an explicit treatment of (topographical) soil moisture when studying drought impacts.

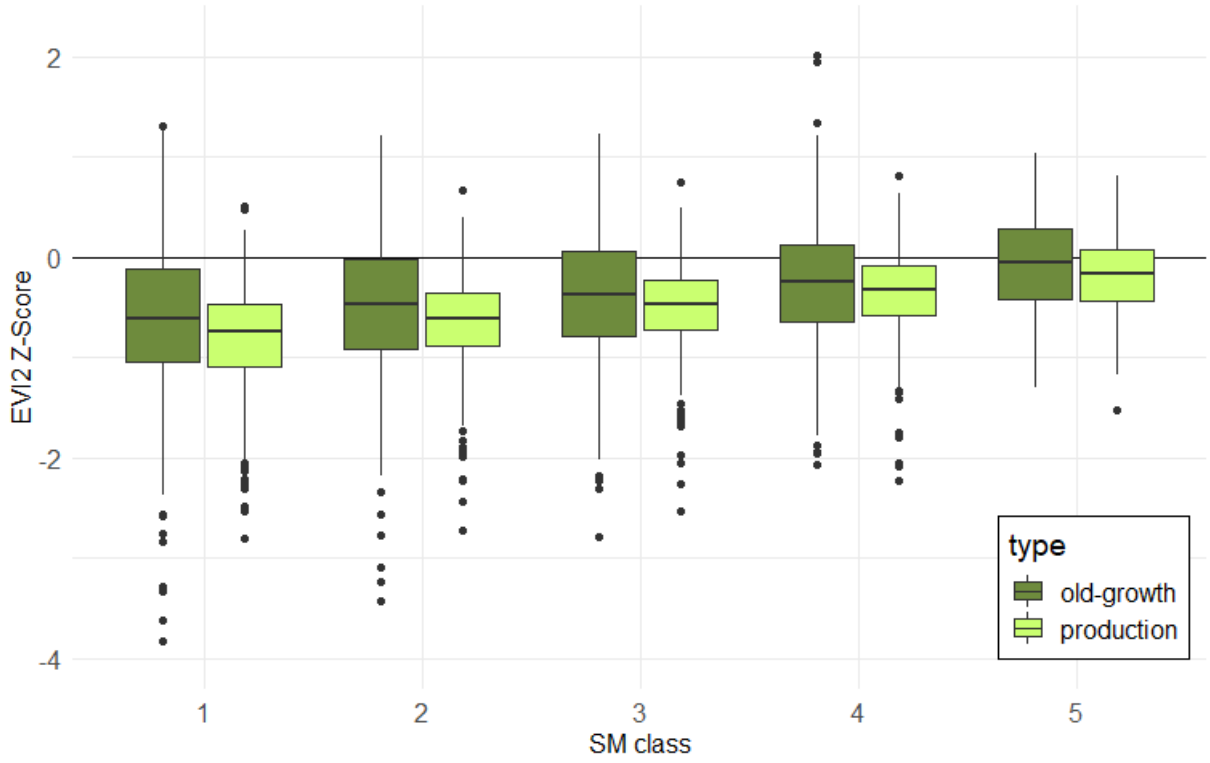

Figure 10: Boxplots providing an overview of the distribution in Z-scores for old-growth and production forests, for each of the five soil moisture (SM) classes. As shown here, with increasing topographical soil moisture, EVI2 Z-scores increase. While old-growth forests are overall less negatively impacted than production forests, their variability in impacts is also higher, and consequently, both the highest and lowest Z-scores are found in this forest type.

Moreover, variability in Z-scores was found to be higher for old-growth than production forests (see boxplot whiskers in Figure 10). Consequently, both the most negatively (- 3.83, SM class 1) and the most positively (+2.00, SM class 4) impacted forests are old-growth stands. Figure 11 further illustrates this, where values above the 1:1 line in the scatterplots are associated with a relatively higher Z-score in the production forest, and vice versa.

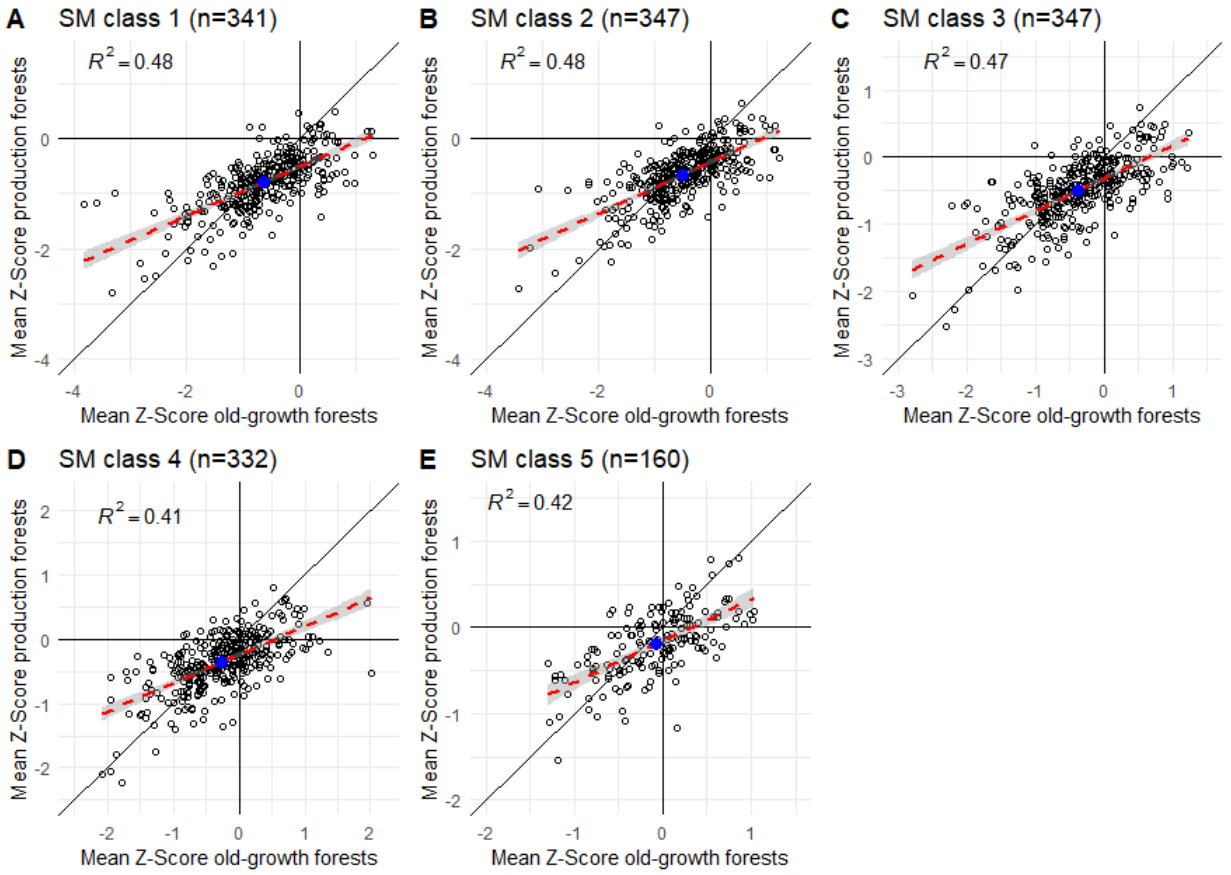

Figure 11: Scatterplots of EVI2 Z-scores of all forest pairs and associated regression lines (dashed red), for the five soil moisture (SM) classes of ascending wetness (**A-E**). A value above the 1:1 line (black) suggest a relatively higher Z-score associated with the production forest in the pair, whereas values below the line are associated with a higher value of the old-growth forest. Blue dots indicate the location of the mean Z-scores of all pairs combined. Note the differing axis-limits of the plots.

4.2.2. Spatial distribution of drought impacts

As illustrated in Figure 12A, the most negatively impacted areas of productive forest land are found in direct vicinity to the southern coastline and on the islands of Öland and Gotland, as well as in the southeastern provinces (Småland, Östergötland, Södermanland, Uppland). Furthermore, in northern Sweden, wide stretches of central Lapland are negatively impacted, with additional, locally impacted areas found scattered across the country (e.g. northern Dalarna). In contrast, positive anomalies are found further inland in southern Sweden (Bohuslän, Värmland), along the northern part of the Bothnian coastline (Norrbotten, Västerbotten), and in the mountains near the Norwegian border (western Lapland). Nevertheless, overall EVI2 Z-scores of all productive forest land are negative, with a mean (± SD) of -0.584 ± 1.31.

Figure 12B illustrates the spatial distribution of the forest pair difference in Z-scores (old-growth – production), which were individually calculated for all five SM classes and subsequently normalized by the frequency distribution of the SM classes across all productive forest land (Figure

12C). When normalized by SM class frequency distributions, the overall mean difference between the forest pairs amounts to +0.130. As shown, five of the 27 old-growth forests that were considerably more negatively impacted than their associated production forests (relative difference in Z-score < -0.5) are found in direct vicinity of the southern coastline, five are found around Dalarna, four along the Bothnian coastline, and the remainder scattered across Norrland. In contrast, the 62 forest pairs in which old-growth forests were considerably less impacted than their production forest buffer (relative difference in Z-score >0.5) are scattered across the entire country.

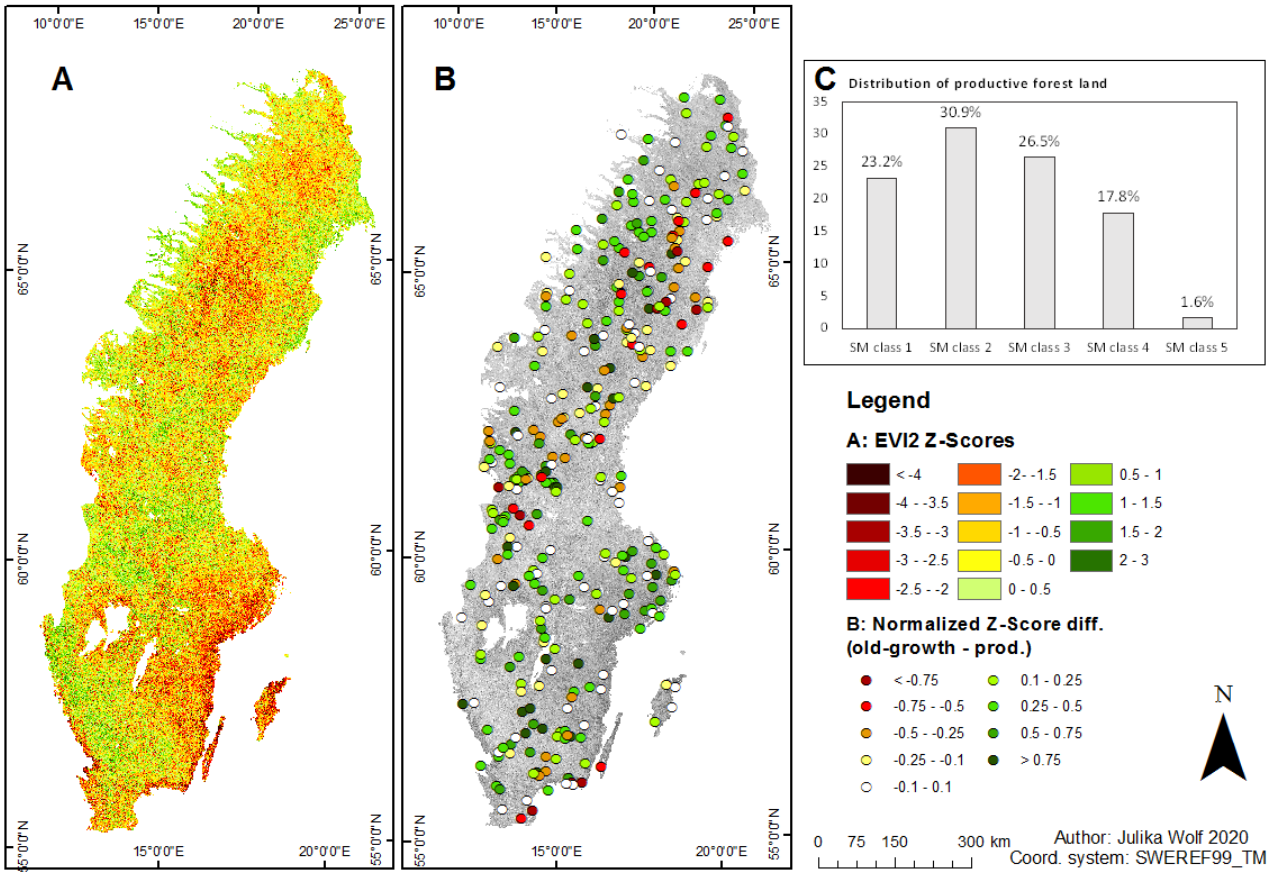

Figure 12: Overview maps of the spatial distribution of drought impacts. **A.** 2018 EVI2 Z-scores for all productive forest land. **B.** Distribution of the relative difference in Z-scores (old-growth – production) of all forest pairs, all soil moisture (SM) classes combined and normalized by their frequency of occurrence. **C.** Frequency distribution of the five SM classes within productive forest land

4.2.3. Potential explanatory variables

Drought severity as indicated by scPDSI was most extreme in the Boreo-Nemoral Zone (mean ± SD: -2.58 ± 0.75, see Figure 13 for the boundaries of the three vegetation zones and gridded scPDSI values). The Boreo-Nemoral Zone is also the zone with the lowest mean EVI2 Z-scores (old-growth: -0.61, production: -0.84). However, neither Z-scores of old-growth and production forests

separately, nor their relative differences (old-growth – production), were found to be linearly related to scPDSI values, irrespective of vegetation zone (Figures 14-16). For both the Boreal Zone and the North Boreal / Alpine Zone, Z-scores were found to decrease with increasing latitude (Boreal: production: adjusted R^2 = 0.26, old-growth: R^2 = 0.14; North Boreal / Alpine: production: R^2 = 0.18, old-growth: no linear relationship). Elevation had contrasting effects on Z-scores, depending on the vegetation zone: in the Boreo-Nemoral Zone, old-growth and production Z-scores showed weak, but significant positive relationships to elevation (production: R^2 = 0.07, old-growth: R^2 = 0.19), while production forest Z-scores decreased with increasing elevation in the North Boreal / Alpine Zone (R^2 = 0.24), and to a lesser extent in the Boreal Zone (R^2 = 0.07). Similarly, the effect of stand age was found to contrast between vegetation zones, with older production forests showing lower Z-scores (R^2 = 0.22) in the Boreo-Nemoral Zone, while in the North Boreal / Alpine Zone, both productive (R^2 = 0.26) and old-growth forests (R^2 = 0.25) displayed positive relationships with stand age. Lastly, production forest Z-scores in the North Boreal / Alpine Zone were found positively related to slope (R^2 = 0.42), while no relationship between slope and Z-scores was found within the other vegetation zones.

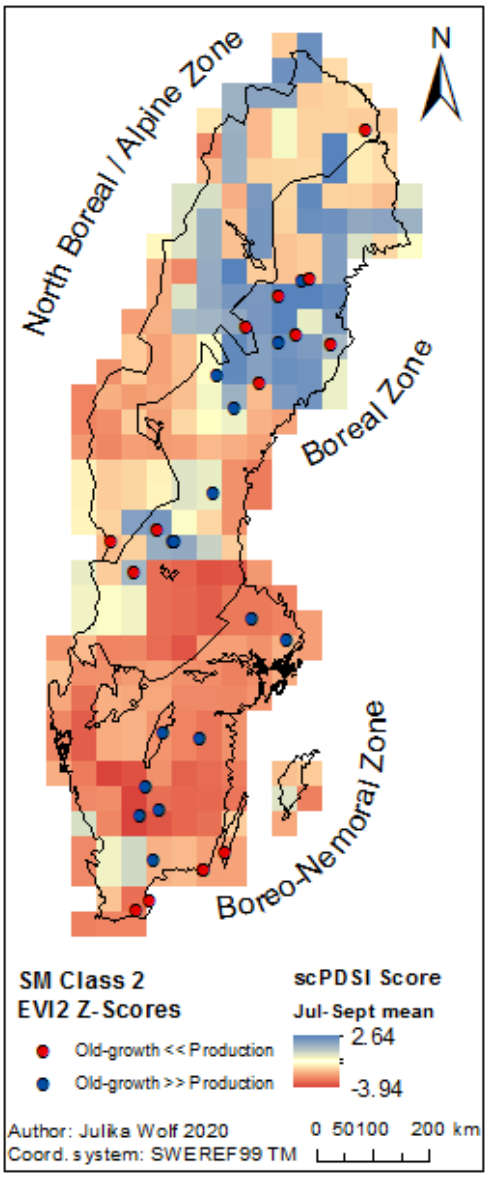

Figure 13: Overview of gridded 2018 July-Sept. scPDSI values, division of dataset into major vegetation zones, and location of the 15 forests pairs with the largest negative (old-growth << prod.) and positive EVI2 Z-score differences in SM Class 2.

While old-growth forests in SM class 2 are significantly older (mean difference ± SD: 21.3y ± 14.13), are located at higher elevations (33.08m ± 57.29), and are found on steeper slopes (1.18° ± 2.40) than their surrounding production forests, the forest-pair differences in stand age, elevation, and slope showed no linear relationship to Z-score differences in either of the three vegetation zones (Figure 14C – 16C). To further investigate this, differences in stand age, elevation, and slope were also analyzed for the 15 largest positive (old-growth >> production) and negative outliers by means of boxplots (Figure 17A). Within forest pairs constituting positive outliers (old-growth >> production), old-growth forests were found to be significantly older than their surrounding production forests (mean difference: 27y). On average, they are also located at slightly lower elevations, but no significant

differences for either elevation or slope are present (Figure 17B). Within the forest pairs constituting the largest negative outliers (old-growth << production), old-growth forests are also significantly older, but the age difference is smaller (mean difference: 17y) than was the case for the positive outliers. Furthermore, old-growth forests within the negative outlier group are found on significantly steeper slopes than their surrounding production forests, as well as on slightly higher elevations, the latter being non-significant.

Lastly, differences in the fraction of forest type (deciduous, mixed, mixed coniferous, spruce, pine) were analyzed. In general, old-growth forests have significantly lower fractions of deciduous and mixed forests; however, mean differences in fractions for those forest types (-0.02 and -0.05, respectively) are small. There is no significant difference in mixed coniferous forests, but old-growth forests contain a significantly lower fraction of pine (mean difference: -0.11) and significantly higher fraction of spruce stands (mean difference: 0.16) than their surrounding production forests (Figure 17C). Within the largest positive outliers, old-growth forests have a slightly, but significantly lower fraction of deciduous stands, while there is no difference in mixed and mixed coniferous fractions, and they also have higher mean fractions of spruce, as well as lower mean fractions of pine, but the latter two differences are insignificant. In contrast, within the largest negative outliers, old-growth forests have a significantly lower fraction of mixed forest, while differences in the remaining forest type fractions were found insignificant; however, it should be noted that variability within the fraction of deciduous stands is high, and those found along the southern shoreline (n=5) do have a significantly larger fraction of deciduous stands than their surrounding production forest.

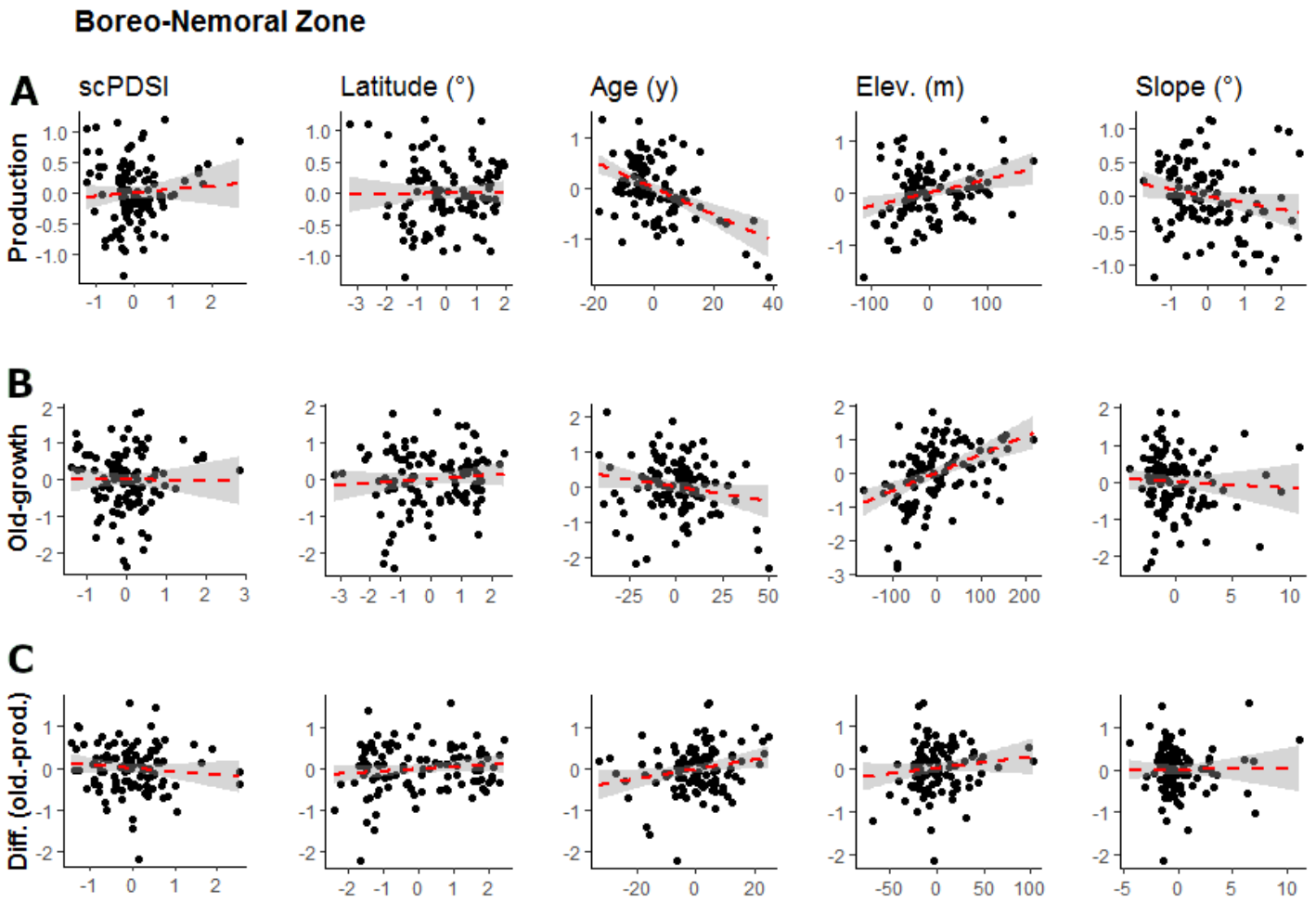

Figure 14: Partial regression plots of forest pairs located in the Boreo-Nemoral Zone (n = 107), showing the general relationship between different environmental variables on **A.** Production forest and **B.** Old-growth forest EVI2 Z-score residuals separately, while **C.** displays the relationship between differences in Z-scores (old-growth – production). As shown, production forest Z-scores show a negative relationship with stand age ($R^2 = 0.22$, $p < 0.001$), which is not the case in old-growth forests. Both production ($R^2 = 0.07$, $p < 0.001$) and old-growth forest Z-scores ($R^2 = 0.19$, $p < 0.001$) show weak, positive relationships with elevation.

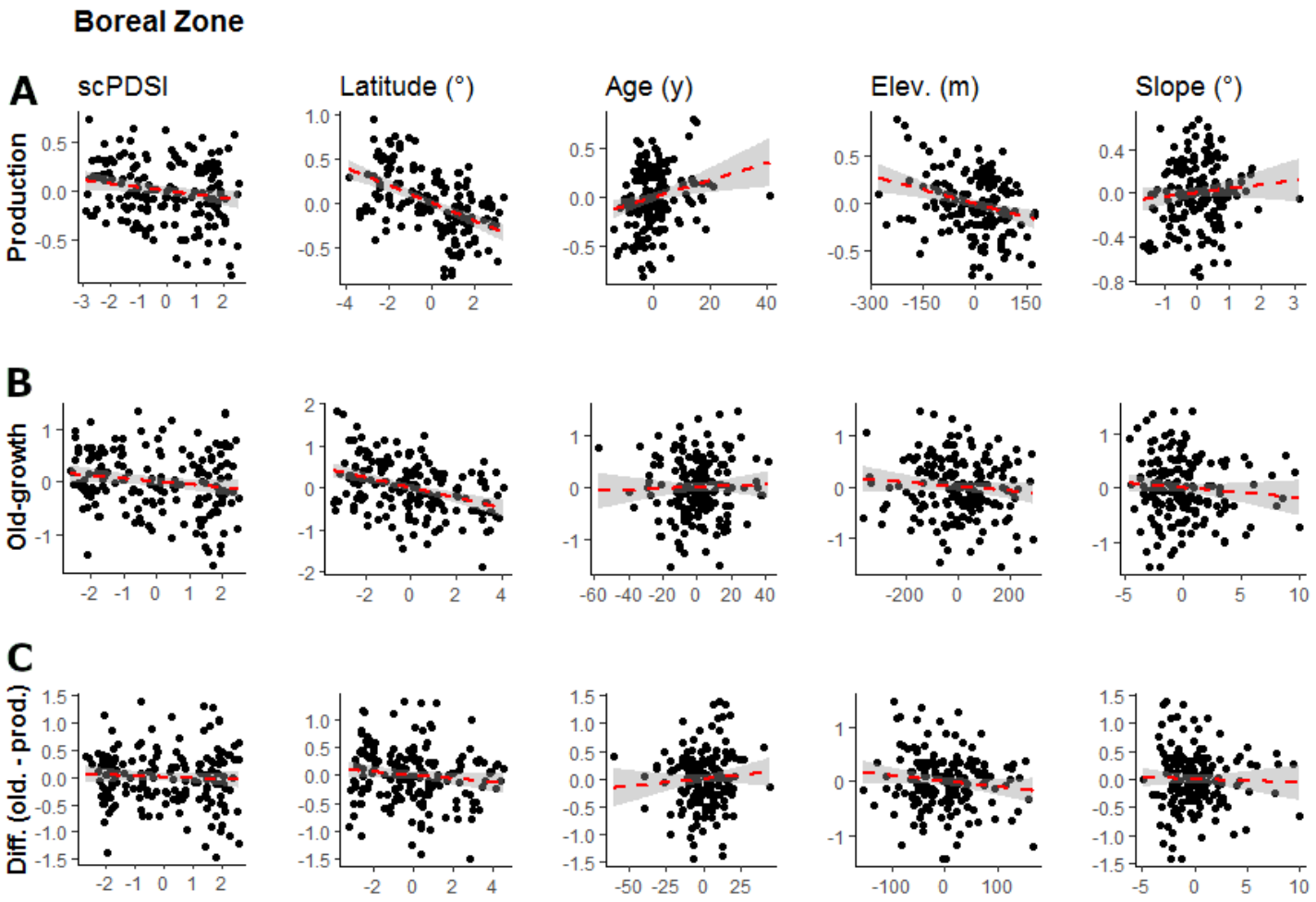

Figure 15: Partial regression plots of forest pairs located in the Boreal Zone (n = 169), showing the general relationship between different environmental variables on **A.** Production forest and **B.** Old-growth forest EVI2 Z-score residuals separately, while **C.** displays the relationship between differences in Z-scores (old-growth – production). As shown, both production ($R^2 = 0.26$, $p < 0.001$) and old-growth forests ($R^2 = 0.14$, $p < 0.001$) show negative relationships with latitude, and production forests show a weak, negative relationship with elevation ($R^2 = 0.07$, $p < 0.001$).

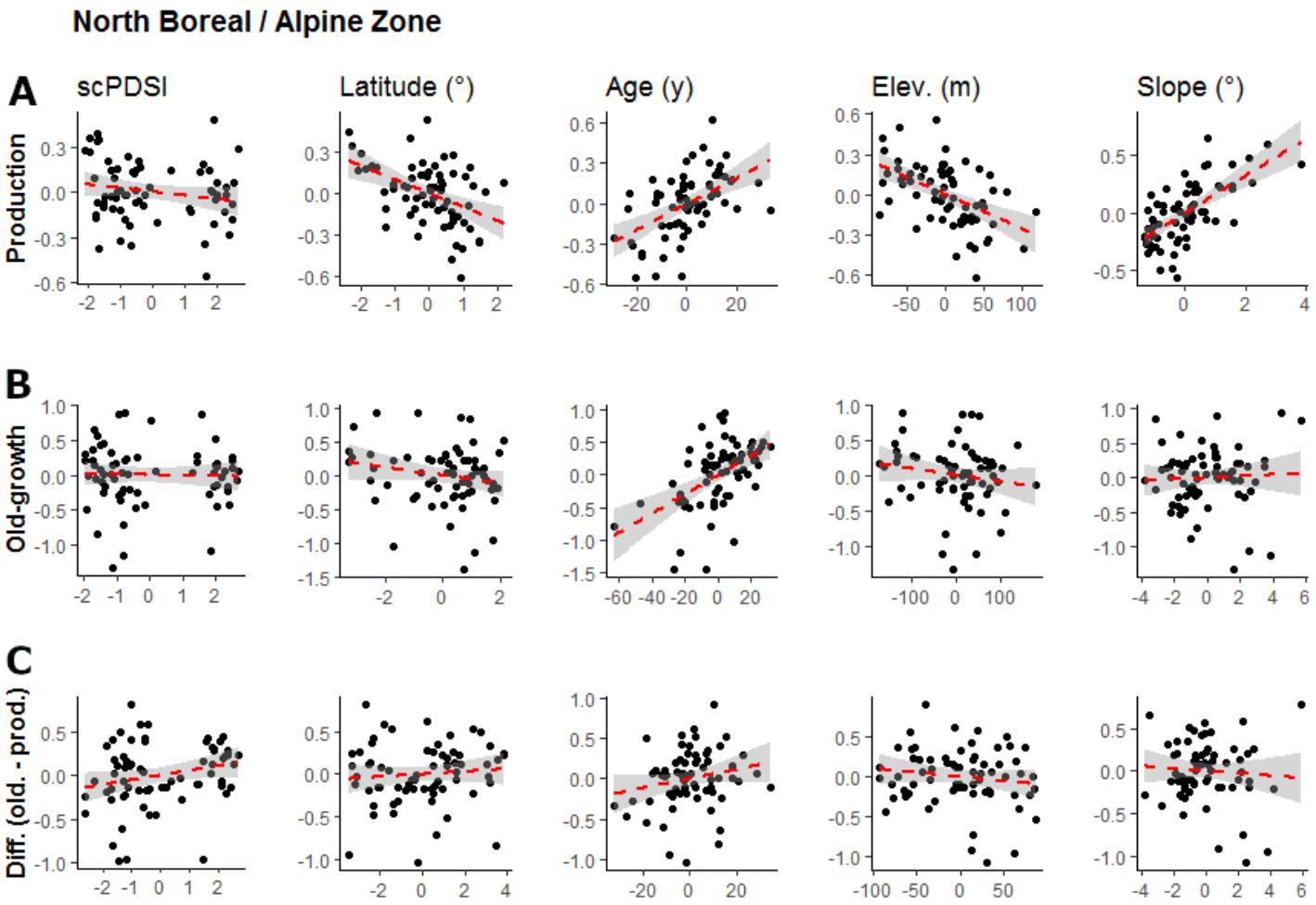

Figure 16: Partial regression plots of forest pairs located in the North Boreal / Alpine Zone (n = 68), showing the general relationship between different environmental variables on **A.** Production forest and **B.** Old-growth forest EVI2 Z-score residuals separately, while **C.** displays the relationship between differences in Z-scores (old-growth – production). As shown, both production ($R^2 = 0.26$, $p < 0.001$) and old-growth ($R^2 = 0.25$, $p < 0.001$) forest Z-scores show positive relationships with stand age. Furthermore, production forest Z-scores are negatively related to latitude ($R^2 = 0.18$, $p < 0.001$) and elevation ($R^2 = 0.24$, $p < 0.001$), and positively to slope ($R^2 = 0.42$, $p < 0.001$), with is neither the case for old-growth forests nor for forest pair Z-score differences.

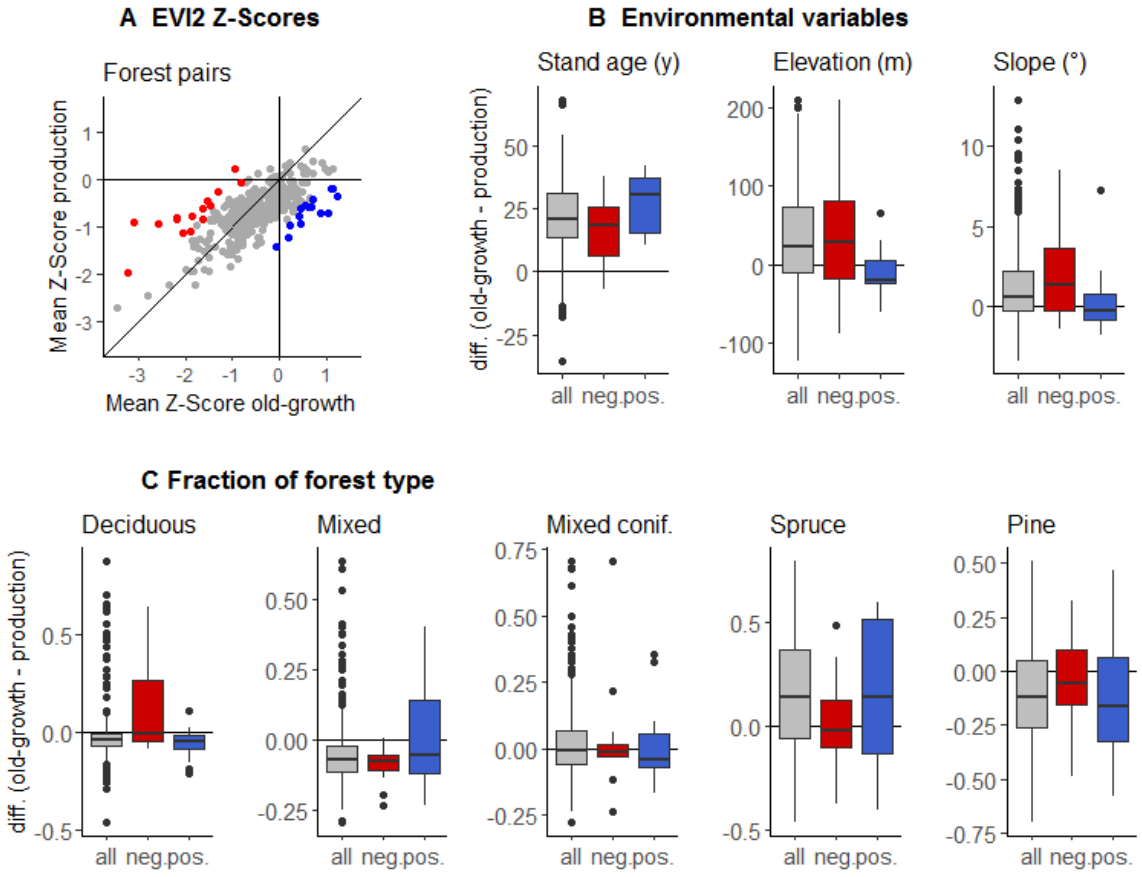

Figure 17: A. Scatterplot highlighting those EVI2 Z-scores associated with the 15 largest positive (old-growth >> production, blue) and negative (old-growth << production, red) outliers found in SM Class 2. **B.** Distribution of the difference (old-growth – production) in **s**tand age, elevation, and slope for all forest pairs (grey) and the 15 most negative (red) and positive (blue) outliers. **C.** Distribution of differences in fractions of forest types.

5. Discussion

5.1. Studying drought impacts with RS data

Given the prospect of more frequent summer dry spells in the years to come, whether old-growth forests are in fact more drought resistant than comparable forests that are extensively managed for production purposes, constitutes a research gap of pivotal urgency, and studies conducted thus far have largely focused on in-situ analyses of differences within production forests, such as the comparison of tree rings within individual forest stands. In contrast to this, this study aimed to investigate the impacts of the 2018 summer drought on Swedish old-growth and production forests through the use of high-resolution remote sensing data and a novel, pair-wise analysis of over 300 old-growth forest stands and their surrounding production forests scattered across the entire

country. To our knowledge, such an approach to studying drought resistance, that is, the ability of a forest to withstand a drought during its occurrence, has never been implemented before, therefore providing a valuable, larger-scale perspective, which can be viewed as complementary to more detailed in-situ studies, as done by, for instance Grossiord et al. (2013).

Perhaps this study's main limitation, and thus uncertainty, is the use of seasonal (July-September) median EVI2 composite values to detect drought stress, which constitutes a relatively blunt tool to study a phenomenon that dynamically evolves over time. The choice of such method was based on the current lack of a better suited satellite product that is able to provide the necessary spatial resolution to study Sweden's highly topographically variable forest landscape, alongside a long enough timeline to establish pre-drought baseline conditions. Currently, only the Landsat 7 and 8 archive meets these criteria, meaning that one has to deal with its inherent drawbacks, such as the diminished scene quality associated with the Landsat 7 ETM+ scanline failure (NASA 2020), as well as the long return time of 16 days per satellite, making data loss due to clouds an issue, as was the case for parts of central Sweden for the month of August. Other studies have solved this through the use of, for instance, a manually selected individual scene found to be completely cloud-free (e.g. Huang and Anderegg 2011), or resorted to coarse-resolution MODIS data whose daily availability allows for shorter-period maximum-value compositing and the use of function-fitting methods (e.g. Cai et al. 2017), neither of which were viable options in this project. On the other hand, the unique approach of studying drought resistance through the pair-wise analysis taken here has the strength to ameliorate some of the uncertainties associated with remotely sensed data, since impacts are studied as relative differences of Z-scores for spatially proximate forests, whose values are simultaneously exposed to the same sources of noise, such as atmospheric or sun-angle effects.

To strengthen the validity of the results found based on Landsat data, it would be interesting to reexamine some of the forests using Sentinel-2 data. While atmospherically corrected Sentinel-2 scenes are only available as of 2017, the satellites' high spatial resolution (10m) and more frequent return time (5 days when the twin-satellites are combined), could be used in a complementary way to Landsat data, allowing for a close-up study of how the drought evolved throughout the summer months, without necessarily establishing a pre-drought baseline. Moreover, in contrast to Landsat, Sentinel-2 has the strength of being equipped with additional bands covering the spectral region associated with the vegetation 'red-edge', specifically designed to study vegetation water stress (e.g. Puletti et al. 2019; Zarco-Tejada et al. 2019).

The fact that EVI2 performed poorly in capturing drops in GPP at the monitoring stations, especially at the Hyltemossa site, potentially means that during part two of this study, only those forests at the higher end of water stress levels displayed negative Z-scores, and it is possible that some of the forests showing no change, or even greening due to preceding spring conditions, still experienced elevated stress levels later in the season, leading to a reduction in photosynthesis but

not to detectable changes in radiation absorbed by chlorophyll. Nevertheless, given that both old-growth and production forests are to a large extent comprised of isohydric species displaying similar stress reaction patterns, the pair-wise approach ameliorates this problem to a certain extent. Furthermore, part of the discrepancy between the VIs and GPP could in hindsight simply be due to the methodology chosen; as stated previously, correct modeling of flux tower footprints was outside the scope of this project, and instead, a single-pixel approach was used. However, a follow-up analysis of the Z-score and topographical soil moisture raster data of the monitoring stations revealed that even in the direct vicinity of the flux towers, heterogeneity of soil moisture and Z-scores is observed. For instance, the Hyltemossa tower is located near a small area belonging to the wettest moisture class, which shows positive Z-scores, while bordering a drier area in the West, associated with negative Z-scores of up to -1.4 (Figure 19). This means that the averaging of the Landsat EVI2 data to a resolution resembling MODIS during part 1, which was done to ensure they represent a similar spatial footprint to make them comparable, likely smoothed out the signal. It could be that the reduction in GPP was largely caused by trees within the drier areas surrounding the flux tower, and that Landsat EVI2 performed better in capturing this than the results of part 1 of this study would suggest. Likewise, while the positive GPP anomaly in Norunda was not captured, the follow-up analysis revealed the presence of several larger areas showing positive Z-scores at a distance of about 300m from the tower, which, while not falling within the 250m pixel, could still be within the range of the flux tower footprint, depending on prevailing wind conditions.

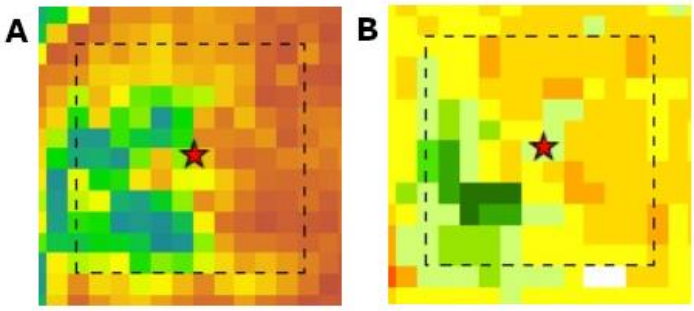

Figure 18: The Hyltemossa flux tower shown as a red star, and a surrounding 250 x 250m zone in dashed. **A.** Soil moisture raster, with wetter classes shown in blue. **B.** Landsat EVI2 Z-scores, with positive anomalies shown in green, and negative anomalies in orange. Note that a single MODIS pixel, corresponding to the size of the dashed square, is unable to capture this.

5.2. Potential reasons for the differences in drought resistance

This study found that Swedish old-growth forests are on average associated with significantly higher EVI2 Z-Scores than comparable production forests, suggesting that old-growth forests were in fact more drought resistant during the summer of 2018. However, why this is the case is unclear, as it is not readily reconcilable by any of the explanatory variables tested. Importantly, positive

differences in Z-scores (old-growth – production) were scattered across all vegetation zones within the entire country and were unrelated to scPDSI drought severity, thus making it a general phenomenon rather than limiting it to certain areas.

When studying old-growth and production forests separately for the three vegetation zones, a few general trends did emerge, most notably in connection to stand age: production forest Z-scores were negatively related to stand age within the Boreo-Nemoral Zone, the region affected most severely by the drought, whereas the opposite was the case in the North Boreal / Alpine Zone. Relating stand age to drought resistance is far from straightforward, and the results highlight this complexity: while in severely dry areas, older trees are likely more vulnerable to xylem tissue damage (see section 2.3), the opposite might be the case in less severely affected areas, where the deeper rooting system of older trees provides access to deeper soil water, and this could potentially explain these contrasting findings. It should be noted that the youngest trees (trees smaller than 5m), classified as 'temporarily no forest' in the land cover raster used, were excluded from the analysis, and it is likely that the highest impacts are in fact found among the very youngest trees.

However, stand age differences did not hold any generalizable explanatory power for differences in Z-scores between old-growth and production forests, and in fact, all of the 15 old-growth forests with the largest Z-score differences where significantly older than their productive counterparts.

These old-growth forests, apart from their much older stand age, might potentially have other characteristics for which no data is currently available, and which might have influenced drought resistance, such as the presence or absence of understory key-stone species. Previous research conducted on Swedish Norway spruce forests showed that the common practice of fertilizing young stands leads to significant reductions in understory, most notably leading to substantial loss of lichen and bryophyte cover (Hedwall et al. 2010). At the same time, research on old-growth forests in the Pacific Northwest and in Japan highlight the importance of lichen and bryophyte rainfall interception and water-storage capacity, especially after the occurrence of abrupt, heavy rain fall events (Pypker et al. 2006; Oishi 2018), as was the case in parts of Sweden in August 2018. At the time of this writing, an active field campaign is underway, which will advance the knowledge of local understory and soil characteristics of a subset of the old-growth forests studied, potentially providing additional explanatory power on why the majority of old-growth forests were found less impacted, especially in the drier soil moisture classes.

Old-growth forests also showed a larger variability in impacts than production forests. Why this is the case is unclear; the smaller variability in production forests could potentially be caused by them being comparatively more alike in structure than old-growth forests are. It also could be simply due to their larger area, and the metric chosen to study the impacts, with each forest represented by a single mean Z-score for each individual soil moisture class. While this constitutes the most straightforward way in conducting a pair-wise analysis, it unavoidably smooths out some of the

variability found within the buffer zones even after accounting for potential soil moisture differences. The approach taken in this study therefore should be viewed as representing general trends of what is occurring within the old-growth and production forest buffer zones; for further research, it would be valuable to conduct a more detailed analysis of a subset of old-growth and production forest pairs, based on a large number of randomly chosen individual pixels falling within the forest boundaries, thus going beyond area-wide mean values. Such pixel-based approach likely also yields clearer relationships to the investigated explanatory variables.

While most old-growth forests were found less impacted than their surrounding production forests, some of the worst impacted forests were old-growth, associated with the largest relative difference in negative impacts (old-growth – production). However, this can be partially reconciled by the fact that these forests are located on significantly steeper slopes, which influences water dynamics; slope steepness has previously been linked to drought-induced forest mortality (Huang and Anderegg 2011). Moreover, all five of the largest outliers in the South of Sweden have a significantly higher fraction of deciduous trees than the surrounding production forests, therefore limiting their comparability. Lastly, while most of Sweden's forests are coniferous, the detailed analysis of soil moisture class 2 revealed that old-growth forests have a significantly higher fraction of pure spruce stands, and less pine; spruce is generally associated with higher vulnerability to droughts, and the Swedish Commission on Climate and Vulnerability (2007) in fact recommends to switch from spruce to pine production to prepare for a drier future climate in southern Sweden. The increased fraction of pure spruce in old-growth forests, in combination with their older age, is therefore quite intriguing, and the separate pixel-wise comparison, as recommended above, in combination with a separate investigation of spruce and pine, has the potential to shed further light on this.

5.4. A cautionary note on spatial scale

Drought impacts were found to depend on a forest stand's topographical soil moisture. The fact that forests located along drier slopes are more impacted by precipitation deficits than those within moist valleys should come as little surprise. However, a high spatial resolution is required to correctly capture this effect. If this is ignored and instead it is assumed *a priori* that it would suffice to proceed with a coarser resolution to study drought impacts, a potentially severe smoothing effect is introduced when pixels associated with wetter sites show positive Z-scores, while being directly adjacent to negatively impacted pixels associated with drier sites, as was shown for Skuleskogen and Hyltemossa. Consequently, when using an inadequate spatial resolution, these values can cancel each other out, and no change is detected at all. How severe this issue is still needs further

consideration, and it would be valuable for future research to explicitly investigate this, through for instance repeated resampling of Landsat data to mimic an increasingly degraded resolution.

In light of these findings, the validity of some of the results of previous drought impact studies based on MODIS data are questionable, such as those by Reinermann et al. (2019), which found no negative deviations in EVI values for forests in Germany during the 2018 drought. Consequently, the authors concluded that this might be due to trees reaching deeper soil water than other land cover types, despite the fact that at the same time several major German newspapers covered reports by the German Forestry Union about the desiccation and subsequent death of over 300 million young trees, as well as a total affected area of 600,000ha, representing unprecedented damage in German forestry history (BDF 2018). It should be noted that most of Germany's continuous stretches of forest coincide with comparatively mountainous terrain, somewhat similar to the type of topography found in Sweden; the findings of this project therefore provide a potential explanatory pathway for the absence of any drought signal detected by Reinermann et al. (2019).

6. Conclusion

This study showed that during the summer drought of 2018, Swedish old-growth forests were on average more drought resistant than production forests, despite their older age, and that differences in resistance decreased with increasing topographical soil moisture. Lastly, what ultimately matters for forest resilience is not necessarily the immediate impact a drought exerts on an ecosystem, but rather the systems' ability to quickly recover and return to pre-drought conditions. As noted earlier, forest mortality has previously been observed to only peak several years post-drought (Anderegg et al. 2019). Therefore, the fact that most old-growth forests were found less impacted than production forests can be viewed as an early warning metric of what might be happening in the years to come. Subsequent continued monitoring, both through collection of field data on, for instance, the percentage of canopy dieback within individual pixels, following a similar procedure as in Huang and Anderegg (2011), as well as through continued remote sensing to detect any future trends, is therefore key to establish whether the majority of old-growth forests are not just more resistant, but also truly more resilient.

References

AghaKouchak, A., A. Farahmand, F. S. Melton, J. Teixeira, M. C. Anderson, B. D. Wardlow, and C. R. Hain. 2015. Remote sensing of drought: Progress, challenges and opportunities. *Reviews of Geophysics,* 53**:** 452-480. DOI: 10.1002/2014rg000456

Ahlström, A., and G. E. de Jong. 2020. Swedish primary forest map.

Ahlström, A., G. E. de Jong, W. Nijland, and T. Tagesson. 2020. Primary productivity of managed and pristine forests in Sweden. *Environmental Research Letters*.

Anderegg, W. R. L., L. D. L. Anderegg, and C. Y. Huang. 2019. Testing early warning metrics for drought-induced tree physiological stress and mortality. *Glob Chang Biol,* 25**:** 2459-2469. DOI: 10.1111/gcb.14655

Anderegg, W. R. L., A. G. Konings, A. T. Trugman, K. Yu, D. R. Bowling, R. Gabbitas, D. S. Karp, S. Pacala, et al. 2018. Hydraulic diversity of forests regulates ecosystem resilience during drought. *Nature,* 561**:** 538-541. DOI: 10.1038/s41586-018-0539-7

Barichivich, J., T. J. Osborn, I. Harris, G. van der Schrier, and P. D. Jones. 2018. Drought [in "State of the Climate in 2018"]. *Bulletin of the American Meteorological Society*

BDF. 2018. Deutschland fehlen 10.000 Forstleute [Germany is lacking 10,000 foresters]. Retrieved 8 July 2020, from https://www.bdf-online.de/aktuelles/news/deutschlandfehlen10000forstleute/.

Belyazid, S., and Z. Giuliana. 2019. Water limitation can negate the effect of higher temperatures on forest carbon sequestration. *European Journal of Forest Research,* 138**:** 287-297. DOI: 10.1007/s10342-019-01168-4

Buchwald, E., 2005. A hierarchical terminology for more or less natural forests in relation to sustainable management and biodiversity conservation. Report, Rome, 11-19 pp.

Buras, A., A. Rammig, and C. S. Zang. 2020. Quantifying impacts of the drought 2018 on European ecosystems in comparison to 2003. *Biogeosciences,* 17**:** 1655-1672. DOI: 10.5194/bg-2019-286

Cai, Z., P.-O. Jönsson, H. Jin, and L. Eklundh. 2017. Performance of Smoothing Methods for Reconstructing NDVI Time-Series and Estimating Vegetation Phenology from MODIS Data. *Remote Sensing,* 9. DOI: 10.3390/rs9121271

CEMS. 2019. Global Drought Observatory timeseries graphs. Retrieved May 18, 2020, from https://edo.jrc.ec.europa.eu/edov2/php/index.php?id=1141.

Cheng, Y.-B., S. Wharton, S. L. Ustin, P. J. Zarco-Tejada, M. Falk, and K. T. Paw U. 2007. Relationships between Moderate Resolution Imaging Spectroradiometer water indexes and tower flux data in an old growth conifer forest. *Journal of Applied Remote Sensing,* 1. DOI: 10.1117/1.2747223

Choat, B., S. Jansen, T. J. Brodribb, H. Cochard, S. Delzon, R. Bhaskar, S. J. Bucci, T. S. Feild, et al. 2012. Global convergence in the vulnerability of forests to drought. *Nature,* 491**:** 752-755. DOI: 10.1038/nature11688

Chuvieco, E. 2016. *Fundamentals of Satellite Remote Sensing - An environmental approach*. Boca Raton: CRC Press.

Ciais, P., M. Reichstein, N. Viovy, A. Granier, J. Ogée, V. Allard, M. Aubinet, N. Buchmann, et al. 2005. Europe-wide reduction in primary productivity caused by the heat and drought in 2003. *Nature,* 437**:** 529-533. DOI: 10.1038/nature03972

Commission on Climate and Vulnerability, 2007. Sweden Facing Climate Change—Threats and Opportunities. SOU, Report, Stockholm.

DeLancey, E. R., J. Kariyeva, J. T. Bried, and J. N. Hird. 2019. Large-scale probabilistic identification of boreal peatlands using Google Earth Engine, open-access satellite data, and machine learning. *PLoS One,* 14**:** e0218165. DOI: 10.1371/journal.pone.0218165

Dotzler, S., J. Hill, H. Buddenbaum, and J. Stoffels. 2015. The Potential of EnMAP and Sentinel-2 Data for Detecting Drought Stress Phenomena in Deciduous Forest Communities. *Remote Sensing,* 7**:** 14227-14258. DOI: 10.3390/rs71014227

Drolet, G. G., K. F. Huemmrich, F. G. Hall, E. M. Middleton, T. A. Black, A. G. Barr, and H. A. Margolis. 2005. A MODIS-derived photochemical reflectance index to detect inter-annual variations in the photosynthetic light-use efficiency of a boreal deciduous forest. *Remote Sensing of Environment,* 98**:** 212-224. DOI: 10.1016/j.rse.2005.07.006

Eriksson, M., L. Samuelson, L. Jagrud, E. Mattsson, T. Celander, A. Malmer, K. Bengtsson, O. Johansson, et al. 2018. Water, Forests, People: The Swedish Experience in Building Resilient Landscapes. *Environ Manage,* 62**:** 45-57. DOI: 10.1007/s00267-018-1066-x

European Commission. 2020. EDO Indicator Factsheet: Standardized Precipitation Index (SPI). Retrieved, from https://edo.jrc.ec.europa.eu/documents/factsheets/factsheet_spi.pdf.

FAO, 2015. Global Forest Resources Assessment 2015. Terms and Definitions., FAO, Report, Rome, 36 pp.

Filella, I., A. Porcar-Castell, S. Munné-Bosch, J. Bäck, M. F. Garbulsky, and J. Peñuelas. 2009. PRI assessment of long-term changes in carotenoids/chlorophyll ratio and short-term changes in de-epoxidation state of the xanthophyll cycle. *International Journal of Remote Sensing,* 30**:** 4443-4455. DOI: 10.1080/01431160802575661

Forrester, D. I., D. Bonal, S. Dawud, A. Gessler, A. Granier, M. Pollastrini, C. Grossiord, and J. Finn. 2016. Drought responses by individual tree species are not often correlated with tree species diversity in European forests. *Journal of Applied Ecology,* 53**:** 1725-1734. DOI: 10.1111/1365-2664.12745

Fridman. 2000. Conservation of forests in Sweden: a strategic ecological analysis. *Biological Conservation*.

Friedlingstein, P., M. W. Jones, amp, apos, M. Sullivan, R. M. Andrew, J. Hauck, G. P. Peters, et al. 2019. Global Carbon Budget 2019. *Earth System Science Data,* 11**:** 1783-1838. DOI: 10.5194/essd-11-1783-2019

Gamon, J. A., K. F. Huemmrich, C. Y. Wong, I. Ensminger, S. Garrity, D. Y. Hollinger, A. Noormets, and J. Penuelas. 2016. A remotely sensed pigment index reveals photosynthetic phenology in evergreen conifers. *Proc Natl Acad Sci U S A,* 113**:** 13087-13092. DOI: 10.1073/pnas.1606162113

Gamon, J. A., L. Serrano, and J. S. Surfus. 1997. The Photochemical Reflectance Index: An Optical Indicator of Photosynthetic Radiation UseEfficiency across Species, Functional Types, and Nutrient Levels. *Springer,* 112**:** 492-501.

Gauthier, S., P. Bernier, T. Kuuluvainen, A. Z. Shvidenko, and D. G. Schepaschenko. 2015. Global forest health and global change. *Science,* 349**:** 819-822. DOI: 10.1126/science.aaa9092

Gazol, A., J. J. Camarero, and L. Gomez-Aparicio. 2016. Functional diversity enhances silver fir growth resilience to an extreme drought. *Journal of Ecology,* 104**:** 1063-1075. DOI: 10.1111/1365-2745.12575

Gorelick, N., M. Hancher, M. Dixon, S. Ilyushchenko, D. Thau, and R. Moore. 2017. Google Earth Engine: Planetary-scale geospatial analysis for everyone. *Remote Sensing of Environment,* 202**:** 18-27. DOI: 10.1016/j.rse.2017.06.031

Grossiord, C., A. Granier, A. Gessler, T. Jucker, and D. Bonal. 2013. Does Drought Influence the Relationship Between Biodiversity and Ecosystem Functioning in Boreal Forests? *Ecosystems,* 17**:** 394-404. DOI: 10.1007/s10021-013-9729-1

Grossiord, C., A. Granier, S. Ratcliffe, O. Bouriaud, H. Bruelheide, E. Checko, D. I. Forrester, S. M. Dawud, et al. 2014. Tree diversity does not always improve resistance of forest ecosystems to drought. *Proc Natl Acad Sci U S A,* 111**:** 14812-14815. DOI: 10.1073/pnas.1411970111

Hansen, M. C., P. V. Potapov, R. Moore, M. Hancher, S. A. Turubanova, A. Tyukavina, D. Thau, S. V. Stehman, et al. 2013. High-Resolution Global Maps of21st-Century Forest Cover Change. *Science,* 342 850-853.

Hedwall, P.-O., A. Nordin, J. Brunet, and J. Bergh. 2010. Compositional changes of forest-floor vegetation in young stands of Norway spruce as an effect of repeated fertilisation. *Forest Ecology and Management,* 259**:** 2418-2425. DOI: https://doi.org/10.1016/j.foreco.2010.03.018

Hernández-Clemente, R., R. M. Navarro-Cerrillo, L. Suárez, F. Morales, and P. J. Zarco-Tejada. 2011. Assessing structural effects on PRI for stress detection in conifer forests. *Remote Sensing of Environment,* 115**:** 2360-2375. DOI: 10.1016/j.rse.2011.04.036

Huang, C. Y., and W. R. L. Anderegg. 2011. Large drought-induced aboveground live biomass losses in southern Rocky Mountain aspen forests. *Global Change Biology,* 18**:** 1016-1027. DOI: 10.1111/j.1365-2486.2011.02592.x

ICOS, D. T. a. I. A. T. C. 2020. Drought-2018 atmospheric CO2 Mole Fraction product for 48 stations (96 sample heights). Retrieved, from

Jacks, G. 2019. Drainage in Sweden -the past and new developments. *Acta Agriculturae Scandinavica, Section B — Soil & Plant Science,* 69**:** 405-410. DOI: 10.1080/09064710.2019.1586991

Jiang, Z., A. Huete, K. Didan, and T. Miura. 2008. Development of a two-band enhanced vegetation index without a blue band. *Remote Sensing of Environment,* 112**:** 3833-3845. DOI: 10.1016/j.rse.2008.06.006

Jonsson, R., G. Egnell, and A. Baudin, 2011. Swedish Forest Sector Outlook. Future Forests Working Report., Report.

Jucker, T., O. Bouriaud, D. Avacaritei, and D. A. Coomes. 2014. Stabilizing effects of diversity on aboveground wood production in forest ecosystems: linking patterns and processes. *Ecol Lett,* 17**:** 1560-1569. DOI: 10.1111/ele.12382

Kokaly, R. F., R. N. Clark, G. A. Swaryze, K. E. Livo, H. T.M., N. C. Pearson, R. A. Wise, W. M. Benzel, et al. 2017. USGS Spectral Library Version 7: U.S. Geological Survey Data Series 1035. 61

DOI: https://doi.org/10.3133/ds1035

KSLA. 2015. Forests and Forestry in Sweden. Retrieved, from https://www.skogsstyrelsen.se/globalassets/in-english/forests-and-forestry-in-sweden_2015.pdf.

Lantmäteriet. 2009. GSD-Elevation data, Grid 50+. Retrieved June 2020, from maps.slu.se.

Lantmäteriet. 2012. GSD Orthophoto 0.5m, RGB. Retrieved June 2020, from maps.slu.get.se.

Lebourgeois, F., N. Gomez, P. Mérian, and P. Pinto. 2013. Mixed stands reduce Abies alba tree-ring sensitivity to summer drought in the Vosges mountains, western Europe. *Forest ecology and management,* 303**:** 61-71. DOI: 10.1016/j.foreco.2013.04.003

Lindahl, K. B., A. Sténs, C. Sandström, J. Johansson, R. Lidskog, T. Ranius, and J.-M. Roberge. 2017. The Swedish forestry model: More of everything? *Forest Policy and Economics,* 77**:** 44-55. DOI: 10.1016/j.forpol.2015.10.012

Linderson, M.-L., J. Holst, M. Heliasz, L. Klemedtsson, A. Klosterhalfen, A. Krasnova, A. Läänelaid, H. Linderson, et al. 2020. Boreal forest carbon exchange and growth recovery after the summer 2018 drought. *EGU General Assembly 2020*. DOI: 10.5194/egusphere-egu2020-10559

Loreau, M., and A. Hector. 2001. Partitioning selection and complementarity in biodiversity experiments. *Nature,* 412**:** 72-76 DOI: 10.1038/35083573

Luyssaert, S., E. D. Schulze, A. Borner, A. Knohl, D. Hessenmoller, B. E. Law, P. Ciais, and J. Grace. 2008. Old-growth forests as global carbon sinks. *Nature,* 455**:** 213-215. DOI: 10.1038/nature07276

Masante, D., and J. Vogt. 2018a. Drought in Central-Northern Europe - July 2018. EDO Analytical Report. Retrieved 30 April 2020, from https://edo.jrc.ec.europa.eu/documents/news/EDODroughtNews201807_Central_North_Europe.pdf.

Masante, D., and J. Vogt. 2018b. Drought in Central-Northern Europe - August 2018. EDO Analytical Report. Retrieved 30 April 2020, from

https://edo.jrc.ec.europa.eu/documents/news/EDODroughtNews201808_Central_North_Europe.pdf.
Masante, D., and J. Vogt. 2018c. Drought in Central-Northern Europe - September 2018. EDO Analytical Report. Retrieved 30 April 2020, from https://edo.jrc.ec.europa.eu/documents/news/EDODroughtNews201809_Central_North_Europe.pdf.
Middleton, E. M., K. F. Huemmrich, D. R. Landis, T. A. Black, A. G. Barr, and J. H. McCaughey. 2016. Photosynthetic efficiency of northern forest ecosystems using a MODIS-derived Photochemical Reflectance Index (PRI). *Remote Sensing of Environment,* 187**:** 345-366. DOI: 10.1016/j.rse.2016.10.021
Mishra, A. K., and V. P. Singh. 2010. A review of drought concepts. *Journal of Hydrology,* 391**:** 202-216. DOI: 10.1016/j.jhydrol.2010.07.012
Mottus, M., L. Aragao, J. Back, R. Hernandez-Clemente, E. E. Maeda, V. Markiet, C. Nichol, R. C. de Oliveira, et al. 2019. Diurnal Changes in Leaf Photochemical Reflectance Index in Two Evergreen Forest Canopies. *IEEE Journal of Selected Topics in Applied Earth Observations and Remote Sensing,* 12**:** 2236-2243. DOI: 10.1109/jstars.2019.2891789
NASA. 2020. Landsat 7. Retrieved, from https://landsat.gsfc.nasa.gov/landsat-7/.
Naturvårdsverket, 1982. URSKOGAR: Inventering av urskogsartade områden i Sverige 1-5
Report, Solna.
Naturvårdsverket. 2019a. Nationella marktäckedata 2018 basskikt [National land cover map 2018 base layer]. Retrieved, from https://gpt.vic-metria.nu/data/land/NMD/NMD_Produktbeskrivning_NMD2018Basskikt.pdf.
Naturvårdsverket. 2019b. Nationella marktäckedata tilläggsskikt produktivitet [National landcover map additional layer for productivity]. Retrieved, from https://gpt.vic-metria.nu/data/land/NMD/NMD_Produktbeskrivning_tillaggsskikt_Produktivitet_v1_0.pdf.
Naturvårdsverket. 2019c. Marktfuktighetsindex [Soil moisture index].
Oishi, Y. 2018. Evaluation of the Water-Storage Capacity of Bryophytes along an Altitudinal Gradient from Temperate Forests to the Alpine Zone. *Forests,* 9. DOI: 10.3390/f9070433
Peters, W., I. R. van der Velde, E. van Schaik, J. B. Miller, P. Ciais, H. F. Duarte, I. T. van der Laan-Luijkx, M. K. van der Molen, et al. 2018. Increased water-use efficiency and reduced CO2 uptake by plants during droughts at a continental-scale. *Nat Geosci,* 11**:** 744-748. DOI: 10.1038/s41561-018-0212-7
Pretzsch, H., G. Schütze, and P. Biber. 2018. Drought can favour the growth of small in relation to tall trees in mature stands of Norway spruce and European beech. *Forest Ecosystems,* 5. DOI: 10.1186/s40663-018-0139-x
Pretzsch, H., G. Schutze, and E. Uhl. 2013. Resistance of European tree species to drought stress in mixed versus pure forests: evidence of stress release by inter-specific facilitation. *Plant Biol (Stuttg),* 15**:** 483-495. DOI: 10.1111/j.1438-8677.2012.00670.x
Puletti, N., W. Mattioli, F. Bussotti, and M. Pollastrini. 2019. Monitoring the effects of extreme drought events on forest health by Sentinel-2 imagery. *Journal of Applied Remote Sensing,* 13. DOI: 10.1117/1.Jrs.13.020501
Pypker, T. G., M. H. Unsworth, and B. J. Bond. 2006. The role of epiphytes in rainfall interception by forests in the Pacific Northwest. I. Laboratory measurements of water storage. *Canadian Journal of Forest Research,* 36**:** 809-818. DOI: 10.1139/X05-298
R Development Core Team. 2013. R: A language and environment for statistical computing
Regeringskansliet. 2019. Lantbruket och torkan [Agriculture and drought]. Retrieved, from https://www.regeringen.se/regeringens-politik/vattenforsorjning-och-torka/lantbruket-och-torkan/.

Reichstein, M., P. Ciais, D. Papale, R. Valentini, S. Running, N. Viovy, W. Cramer, A. Granier, et al. 2007. Reduction of ecosystem productivity and respiration during the European summer 2003 climate anomaly: a joint flux tower, remote sensing and modelling analysis. *Global Change Biology,* 13**:** 634-651. DOI: 10.1111/j.1365-2486.2006.01224.x

Reinermann, S., U. Gessner, S. Asam, C. Kuenzer, and S. Dech. 2019. The Effect of Droughts on Vegetation Condition in Germany: An Analysis Based on Two Decades of Satellite Earth Observation Time Series and Crop Yield Statistics. *Remote Sensing,* 11. DOI: 10.3390/rs11151783

Rosner, S., N. Gierlinger, M. Klepsch, B. Karlsson, R. Evans, S.-O. Lundqvist, J. Světlík, I. Børja, et al. 2018. Hydraulic and mechanical dysfunction of Norway spruce sapwood due to extreme summer drought in Scandinavia. *Forest Ecology and Management,* 409**:** 527-540. DOI: 10.1016/j.foreco.2017.11.051

Sabatini, F. M., S. Burrascano, W. S. Keeton, C. Levers, M. Lindner, F. Pötzschner, P. J. Verkerk, J. Bauhus, et al. 2018. Where are Europe's last primary forests? *Diversity and Distributions,* 24**:** 1426-1439. DOI: 10.1111/ddi.12778

Seidl, R., D. Thom, M. Kautz, D. Martin-Benito, M. Peltoniemi, G. Vacchiano, J. Wild, D. Ascoli, et al. 2017. Forest disturbances under climate change. *Nat Clim Chang,* 7**:** 395-402. DOI: 10.1038/nclimate3303

SLU. 2010. kNN-Sverige - Aktuella kartdata över skogsmarken, årgång 2005 och 2010.

SMHI. 2018a. Somaren 2018 - Extremt varm og solig [Summer 2018 - extremely warm and sunny]. Retrieved 30 April 2020, from https://www.smhi.se/klimat/klimatet-da-och-nu/arets-vader/sommaren-2018-extremt-varm-och-solig-1.138134.

SMHI. 2018b. Månads-, årstids- och årskartor [Monthly, seasonal, and yearly maps]. Retrieved 30 April 2020, from https://www.smhi.se/data/meteorologi/kartor/manadsnederbord-procent-av-normal/arlig/2018.

Tian, F. 2020. Intercalibration procedure for Landsat 5,7, and 8 EVI2.

Tilman, D., F. Isbell, and J. M. Cowles. 2014. Biodiversity and Ecosystem Functioning. *Annual Review of Ecology, Evolution, and Systematics,* 45**:** 471-493. DOI: 10.1146/annurev-ecolsys-120213-091917

Trugman, A. T., M. Detto, M. K. Bartlett, D. Medvigy, W. R. L. Anderegg, C. Schwalm, B. Schaffer, and S. W. Pacala. 2018. Tree carbon allocation explains forest drought-kill and recovery patterns. *Ecol Lett,* 21**:** 1552-1560. DOI: 10.1111/ele.13136

Vanhellemont, M., R. Sousa-Silva, S. L. Maes, J. Van den Bulcke, L. Hertzog, S. R. E. De Groote, J. Van Acker, D. Bonte, et al. 2019. Distinct growth responses to drought for oak and beech in temperate mixed forests. *Sci Total Environ,* 650**:** 3017-3026. DOI: 10.1016/j.scitotenv.2018.10.054

Vestin, P. 2017. Effects of forest management on greenhouse gas fluxes in a boreal forest. PhD Thesis

Wang, L., J. J. Qu, X. Hao, and Q. Zhu. 2008. Sensitivity studies of the moisture effects on MODIS SWIR reflectance and vegetation water indices. *International Journal of Remote Sensing,* 29**:** 7065-7075. DOI: 10.1080/01431160802226034

Wells, N., S. Goddard, and M. J. Hayes. 2004. A Self-Calibrating Palmer Drought Severity Index. *American Meteorological Society,* 17**:** 2335-2350.

Xiong, J., P. S. Thenkabail, M. K. Gumma, P. Teluguntla, J. Poehnelt, R. G. Congalton, K. Yadav, and D. Thau. 2017. Automated cropland mapping of continental Africa using Google Earth Engine cloud computing. *ISPRS Journal of Photogrammetry and Remote Sensing,* 126**:** 225-244. DOI: https://doi.org/10.1016/j.isprsjprs.2017.01.019

Zarco-Tejada, P. J., A. Hornero, P. S. A. Beck, T. Kattenborn, P. Kempeneers, and R. Hernandez-Clemente. 2019. Chlorophyll content estimation in an open-canopy conifer forest with Sentinel-2A and hyperspectral imagery in the context of forest decline. *Remote Sens Environ,* 223**:** 320-335. DOI: 10.1016/j.rse.2019.01.031

Appendix A

Example script used for Landsat EVI2 Z-score computations in Google Earth Engine

```
//this script computes Landsat EVI2 Z-scores within predefined polygons.
//final script created by Julika Wolf, 12 May 2020. Adapted from Landsat timeseries
script provided by Feng Tian.

// import smaller shapefile, retrieve geometry (in SWEREF99-tm), display on map.
var sweden = ee.FeatureCollection('users/julikawolf/sweden4');
sweden = sweden.geometry();
Map.centerObject(sweden);

/*
// Sweden borders, for display purposes only if needed. It replaces the uploaded
smaller shapefile but is too big for download later on.
var sweden = ee.FeatureCollection('USDOS/LSIB_SIMPLE/2017')
  .filterMetadata('country_co', 'equals', 'SW');
*/

//add polygon boundary to map display
Map.addLayer(sweden, {color: 'red'}, 'sweden');

// functions to mask cloud, cloud shadow and snow pixels
var maskL457 = function(image) {
var qa = image.select('pixel_qa');
  var cloud = qa.bitwiseAnd(1 << 5)
                  .and(qa.bitwiseAnd(1 << 7))
                  .or(qa.bitwiseAnd(1 << 3))
                  .or(qa.bitwiseAnd(1 << 4));
  var mask2 = image.mask().reduce(ee.Reducer.min());
  return image.updateMask(cloud.not()).updateMask(mask2);
};

function maskL8(image) {
  // Bits 3, 4 and 5 are cloud shadow, snow and cloud, respectively.
  var cloudShadowBitMask = (1 << 3);
  var snowBitMask = (1 << 4);
  var cloudsBitMask = (1 << 5);
  // Get the pixel QA band.
  var qa = image.select('pixel_qa');
  // Both flags should be set to zero, indicating clear conditions.
  var mask = qa.bitwiseAnd(cloudShadowBitMask).eq(0)
                 .and(qa.bitwiseAnd(snowBitMask).eq(0))
                 .and(qa.bitwiseAnd(cloudsBitMask).eq(0));
  return image.updateMask(mask);
};

// return all Landsat 5 EVI2 summer months (July - Sept)
// and calibrated to Landsat 7 values
var Landsat5 = ee.ImageCollection('LANDSAT/LT05/C01/T1_SR')
                  .filterDate('2008-01-01', '2018-12-31') //baseline years
                  .filter(ee.Filter.calendarRange(7,9,'month'))
                  .filterBounds(sweden)
                  .map(function(img) {return img.clip(sweden)})
                  .map(maskL457)
                  .map(function Landsat5EVI2(image) { //calibrated to fit Landsat 7
                    var EVI2 = image.expression(
                      '2.5 * ((NIR/10000 - RED/10000) / (NIR/10000 + 2.4 * RED/10000 +
1)) * 1.0091249 + 0.007209736', {
                      'NIR': image.select('B4'), 'RED': image.select('B3')
```

```
                    }).rename('EVI2');
                  return image.addBands(EVI2);
                })
                .select(['EVI2']);


// return all Landsat 7 EVI2 summer months (July - Sept)
var Landsat7 = ee.ImageCollection('LANDSAT/LE07/C01/T1_SR')
                .filterDate('2008-01-01', '2018-12-31')
                .filter(ee.Filter.calendarRange(7,9,'month'))
                .filterBounds(sweden)
                .map(function(img) {return img.clip(sweden)})
                .map(maskL457)
                .map(function Landsat7EVI2(image) {
                  var EVI2 = image.expression(
                      '2.5 * ((NIR/10000 - RED/10000) / (NIR/10000 + 2.4 * RED/10000
+ 1))', {
                      'NIR': image.select('B4'), 'RED': image.select('B3')
                      }).rename('EVI2');
                  return image.addBands(EVI2);
                })
                .select(['EVI2']);

// return all Landsat 8 EVI2 summer months
// and calibrated to Landsat 7 values
var Landsat8 = ee.ImageCollection('LANDSAT/LC08/C01/T1_SR')
                .filterDate('2008-01-01', '2018-12-31')
                .filter(ee.Filter.calendarRange(7,9,'month'))
                .filterBounds(sweden)
                .map(function(img) {return img.clip(sweden)})
                .map(maskL8)
                .map(function Landsat8EVI2(image) {
                  var EVI2 = image.expression(
                    '2.5 * ((NIR/10000 - RED/10000) / (NIR/10000 + 2.4 * RED/10000 +
1)) * 0.9475403 - 0.015406447', {
                      'NIR': image.select('B5'), 'RED': image.select('B4')
                      }).rename('EVI2');
                  return image.addBands(EVI2);
                })
                .select(['EVI2']);

var Landsat578 = Landsat5.merge(Landsat7).merge(Landsat8);

print(Landsat578, "landsat578");

// this function filters out values less than 0.15 or larger than 1.0, associated with
remaining clouds or cloud shadows (heuristic approach)
var filterthreshold = function(image) {
  return
image.updateMask(image.select('EVI2').gt(0.15).updateMask(image.select('EVI2').lte(1.0)
));
};

//map threshold filtering over collection
var Landsat578 = Landsat578.map(filterthreshold);

var years = ee.List.sequence(2008, 2018);

// retrieve annual summer median
var Landsat578_summer_median = ee.ImageCollection.fromImages(
  years.map(function(y) {
    return Landsat578
      .filter(ee.Filter.calendarRange(y, y, 'year'))
```

```
      .median()
      .set('year', y);
    })
  )
  .toBands();

//select baseline years 2008-2017
var baseline = Landsat578_summer_median
    .select(['0_EVI2', '1_EVI2', '2_EVI2',
'3_EVI2','4_EVI2','5_EVI2','6_EVI2','7_EVI2','8_EVI2','9_EVI2']);

// Reduce the collection to calculate mean and standard deviation needed for Z-scores
var mean = baseline.reduce(ee.Reducer.mean());
var stdv = baseline.reduce(ee.Reducer.stdDev());
var band2018 = Landsat578_summer_median.select('10_EVI2');

//combine the three bands
var stacked = band2018.addBands(mean).addBands(stdv);
print(stacked, 'stacked');

//compute Z-scores
var zscore = stacked.select('10_EVI2').subtract(stacked.select('mean'))
  .divide(stacked.select('stdDev'));

//visualize as Z-score map
var Viz = {min: -3, max: 3, palette: ['red', 'orange','yellow','green', 'blue']};
Map.addLayer(zscore, Viz);

//export to drive for further processing in ArcGIS
Export.image.toDrive({
  image: zscore,
  description: 'EVI2_sweden4_zscore_growing_median_2008_2018',
  scale: 30,
  maxPixels: 1e13,
  fileFormat: 'GeoTIFF',
  region: sweden
});
```